

Compressive force generation by a bundle of living biofilaments

Sanoop Ramachandran and Jean-Paul Ryckaert*
*Physique des Polymères, Université Libre de Bruxelles,
Campus Plaine, CP 223, B-1050 Brussels, Belgium*
(Dated: August 14, 2018)

To study the compressional forces exerted by a bundle of living stiff filaments pressing on a surface, akin to the case of an actin bundle in filopodia structures, we have performed particulate Molecular Dynamics simulations of a grafted bundle of parallel living (self-assembling) filaments, in chemical equilibrium with a solution of their constitutive monomers. Equilibrium is established as these filaments, grafted at one end to a wall of the simulation box, grow at their chemically active free end and encounter the opposite confining wall of the simulation box. Further growth of filaments requires bending and thus energy, which automatically limit the populations of longer filaments. The resulting filament sizes distribution and the force exerted by the bundle on the obstacle are analyzed for different grafting densities and different sub- or supercritical conditions, these properties being compared with the predictions of the corresponding ideal confined bundle model. In this analysis, non-ideal effects due to interactions between filaments and confinement effects are singled out. For all state points considered at the same temperature and at the same gap width between the two surfaces, the force per filament exerted on the opposite wall appears to be a function of a rescaled free monomer density $\hat{\rho}_1^{\text{eff}}$. This quantity can be estimated directly from the characteristic length of the exponential filament size distribution P observed in the size domain where these grafted filaments are not in direct contact with the wall. We also analyze the dynamics of the filament contour length fluctuations in terms of effective polymerization (U) and depolymerization (W) rates, where again it is possible to disentangle non-ideal and confinement effects.

I. FORCE GENERATION BY A BUNDLE OF PARALLEL LIVING FILAMENTS: INTRODUCTION

The generation of force and work by polymerizing actin filaments pushing on the cell membrane during the development of lamellopodia or filopodia or pushing on a host vesicle in the intracellular matrix (lysteria), has attracted much attention for the last 30 years. [1–3] Biomimetic experiments have recently been set up to probe polymerizing filament networks on systems of controlled complexity which are designed to either probe the polymerization force directly [4, 5] or to indirectly observe confinement effects on growing bundles. [6] The stationary force generated by a single actin filament polymerizing against a wall is established theoretically by invoking some form of ratchet mechanism [1, 7] for the monomer insertion between the tip of the filament and the wall. For a rigid filament hitting the wall normally, the standard result is [1]

$$f_N = \frac{k_B T}{d} \ln \left(\frac{\rho_1}{\rho_{1c}} \right), \quad (1)$$

where d is the incremental contour length per added monomer, ρ_1 the free monomer number density and $\rho_{1c} = 1/K$ the free monomer critical density directly related to the effective equilibrium constant K of the single monomer (de)polymerization reaction taking place at filament ends. This wall equilibrium force is the elementary case of the stalling force, namely the force needed to stop the progression of an arbitrary living filament network implying generally additional filament capping, severing or branching proteins and also the irreversible hydrolysis of ATP-actin complexes.

An interesting challenge of intermediate complexity is provided by the establishment of the force-velocity relationship for a bundle of parallel F-actin filaments which includes the determination of the force needed to stop the growth of the bundle in absence of any interference with additional coupled reactions involving other proteins.

An experimental set up where the rigid polarized acrosome of *Limulus* sperm was used as an actin bundle initiator has been exploited [4] to measure the stationary force exerted by growing filaments on a fixed wall while simultaneously, the number of filaments implicated was independently determined.

The surprising result that the force for a eight-filament bundle is essentially of the order of magnitude of the force in Eq. (1), expected theoretically for a single filament, has been attributed to some dynamic instability-like length

* jryckaer@ulb.ac.be

fluctuations but the interpretation of this, unfortunately unique, experiment is still under debate. [8, 9] Theoretical rationalization in terms of stochastic models of filaments bundles [8, 10, 11] invariably suggest that, in supercritical conditions, the force exerted by a wall to stop a bundle of polymerizing filaments is extensive in the number of filaments. In these stochastic model approaches, some ad hoc choices must be made on how the total load force exerted through the wall on the bundle is shared by the individual filaments touching the wall. Similarly, there is no clear argument to decide how the wall force modifies, separately, the polymerizing rate U and the depolymerizing rate W when the tip of the filament is at contact. These microscopic aspects have however direct implications on the growth kinetics as it was shown explicitly for a dynamical model of a hundred filaments actin bundle pressing on a moving wall. [8] The living filaments are treated as straight rods having fixed parallel orientation and are subject to discrete length fluctuations, some plausible rules being assumed for the (de)polymerizing rates relative to filaments hitting the wall, while the wall position itself is assigned at the tip of the longest filament(s) which can be unique or not, hence the need for the choice of an equal distribution of the total load force among them. Equation (1) is recovered for the stalling force per filament and the velocity-force dynamical behaviour shows a sharp transition between a non-condensed state at small load and a condensed state at higher loads where long filaments accumulate against the piston, the stalling regime being approached very slowly. [8] Another study including lateral attractive interactions between filaments suggests an increase, with respect to Eq. (1), of the equilibrium force exerted by the bundle on the wall. [10] Next to these stochastic models which are either treated analytically (at the price of further approximations) or solved numerically using stochastically generated chemical events using Gillespie algorithm, attempts have been made to undertake a direct Brownian dynamics simulation of monomers at a mesoscopic level for the reacting system composed of filaments and a solution of individual free monomers. Along this approach where some ad-hoc rules are used to describe the self-assembly processes without an explicit consideration to fundamental (non-)equilibrium statistical mechanics aspects, one finds the case of a single living actin filament, [12, 13] and the study of the self-assembly of living filament branched networks pressing on a mobile wall. [14, 15]

Recently, we have proposed a new hybrid Molecular dynamics-Monte-Carlo simulation method sampling a reactive canonical ensemble for systems composed of a fixed number N_f of semi-flexible filaments, modeled by a discrete wormlike chain model, and a solution of free monomers occupying a volume V at temperature T . [16] Under the last ensemble constraint in the reactive system of a fixed total number of monomers N_t , single monomer (de)polymerizing events at filament ends are taking place along the microscopic time trajectory on the basis of an instantaneous Monte-Carlo spatially localized association/dissociation process satisfying micro-reversibility. With some proximity criterium and with some characteristic probability rate, a free monomer attempts an association step at an active end of a filament end while, in parallel, with some related probability rate, any filament end monomer attempts a depolymerization step. Any attempt, implying a topological change in the monomer connectivity within the reacting filament and a very limited spatial shift of the reacting monomer, is then subject to an acceptance probability based on the energy change implied. In case of acceptance, the time trajectory is then the object of a discontinuity related to the instantaneous modifications implied by the accepted chemical step. This method was successfully tested on a solution of living filaments with an artificial size upper limit to test the distribution of filament lengths at equilibrium for various thermodynamic conditions tuned by the set of independent state variables (N_f, N_t, V, T) .

In the present paper, we exploit the above methodology to investigate the equilibrium state of a bundle of N_f filaments of persistence length l_p , grafted at one end to a flat solid surface of area A with their first segment constrained along the surface normal, as illustrated in Fig. 1. A second wall, parallel to the first, with gap distance $L \ll l_p$ is treated as an obstacle to the growth of the bundle's filaments by effective polymerization at their chemically active free end. Individual filaments have thus a contour length L_c limited beyond $L_c \approx L$ by the larger and larger bending energy penalty needed to accomodate longer and longer filament sizes. The Hamiltonian model used is similar to the one exploited for free living filaments in solution [16] with the same intramolecular model and the same treatment of the intermolecular forces but, in the present case, it includes a confinement potential and grafting constraints. The whole system, treated in the canonical reactive ensemble specified by the independent variables (N_f, N_t, A, L, T) , furnishes a variety of thermodynamic, structural and dynamical properties which are detailed in the bulk of this paper.

In the ideal solution approximation where the intermolecular forces in the Hamiltonian are simply turned off, the structural and thermodynamical properties of the same grafted and confined bundle reactive system considered within the same (N_f, N_t, A, L, T) canonical reactive ensemble can be obtained analytically, except for single filament-wall integrals which generally do require single filament Monte-Carlo calculations. [17] This illuminating ideal solution treatment of such a complex system has been developed in detail separately, [17] but is however the object of a short summary in the present paper, given the important role it plays in the guidance of the massive particulate simulations reported here for the first time and in the comparative analysis with the results of corresponding simulations of the non-ideal case. Let us just anticipate here that this theoretical treatment furnishes, in the ideal solution approximation, the filament size distribution and the related average force exerted by such a living filament on the obstacle wall. These properties strongly rely on the already mentioned filament-wall integrals which deal with the effective wall

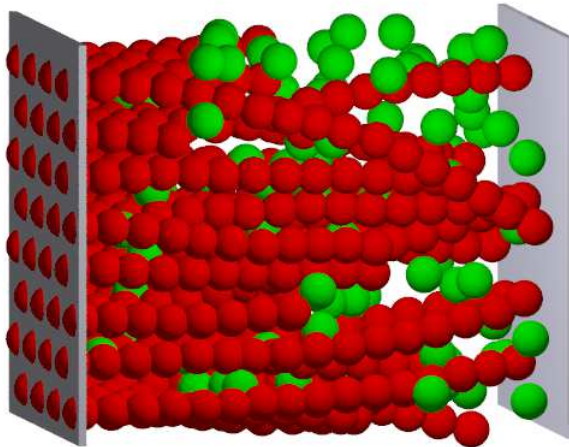


FIG. 1. Simulation box with N_f living filaments (shown in red) anchored normal to the solid wall on the left, in chemical equilibrium with free monomers (shown in green). Single monomer end-filament (de)polymerization take place continuously for a prescribed total number N_t of monomers. The filament growth (in supercritical conditions) is obstructed by the second solid wall on the right which exerts a normal equilibrium force on the bundle. The snapshot shown (note that periodic boundary conditions apply in lateral directions) is extracted from the $N_f = 32, N_t = 500$ case within the IIa experiments series (see Table I).

force and associated mean force potential between a fixed size grafted filament and an obstacle wall located at distance L from the filament grafted end and oriented perpendicularly to the initial end-grafting direction. On the specific single grafted filament-wall topics, let us mention an illuminating study of the interaction between a grafted continuous wormlike chain and a hard wall where universal relations, valid in the stiff limit where $l_p \gg L$, are reported. [18]

The paper is organized as follows: in the first part of Sec. II, we describe a general thermodynamics and statistical mechanics framework in which the properties of our grafted and confined bundle of interacting living filaments can be formulated. We introduce various quantities which are needed to quantify non-ideal effects and confinement properties and define the filament osmotic force concept. In the second part of the same section, we report the most important general properties of the ideal bundle system. The next section, Sec. III, is concerned with the explicit microscopic model which is used in our particulate simulations. We first concentrate in Sec. III A on the single fixed size filament model, including its interaction with the obstacle wall while the global system aspects of the model, including the living filament aspects, are reported in Sec. III B. We finally give in Sec. III C the list of adopted parameters. In Sec. IV, we start by giving the list of experiments organized by increasing grafting density and increasing total number of monomers for a unique set of the other independent variables (L, T) . Results are then presented, regrouped into specific subsections devoted to the different structural and dynamical investigated properties. Finally, Sec. V contains an overall discussion and indicates some perspectives.

II. THERMODYNAMIC DESCRIPTION OF THE CONFINED BUNDLE

A. The general approach

The bundle model detailed in previous section can be described thermodynamically in terms of the Helmholtz free energy $F(T, A, L, N_t, N_f)$ of a closed reacting fluid system at temperature T , having a fixed total number N_t of solute monomers enclosed in a slit pore of transverse area A and gap width L and having N_f permanent filament seeds anchored at one wall giving rise to a bundle of living filaments. These filaments undergo single monomer exchanges at their free end with the free monomers in the bath according to reversible chemical reactions



where A_i and A_1 represent a grafted filament of size i and a free monomer, respectively. The length of a filament of size i is $L_{ci} = (i - 1)d$ where d is the monomer size, more exactly the filament contour length contribution per inserted monomer. This series of reactions (and series of chemical species) is considered as limited to the indicated size window in our theoretical framework. The choice of a minimum size of three monomers is motivated by the

fact that the chemical equilibrium constant associated to the reaction Eq. (2) becomes size independent typically beyond $i = 3$. [1] The neglect of shorter assemblies will be shown to have no impact on our conclusions, a fortiori in supercritical conditions where short filament populations are marginal. The upper limit in the distribution, defined as

$$z^* = \frac{\pi L}{2d}, \quad (3)$$

prevents the occurrence of grafted filaments which, after an initial large amplitude bending, would start growing without further bending energy, parallel to the the obstacle wall. In Eq. (3), z^* corresponds to the size of a filament which can be mapped on a quarter of a circle of radius L , where L is the gap width between the grafting and obstacle planes. Focusing in the present work to the compressive force exerted by a bundle of relatively stiff filaments ($l_p \gg L$), it will be verified later that filaments of size z^* remain practically unpopulated in the supercritical regime as long as the free monomer concentration is appropriately limited. A quantitative assessment of this limit will be given in Eq. (27).

Starting with the general differential form of the free energy for a non- reactive mixture of all species with N_1 free monomers, N_3 trimer filaments, N_4 quadrimer filaments \dots , treated as independent variables, one has

$$dF = -SdT - p_N AdL - p_T LdA + \mu_1 dN_1 + \sum_{i=3}^{z^*} \mu_i dN_i. \quad (4)$$

Here p_N and p_T represent the normal and the tangential pressures respectively and the μ 's are the imposed chemical potentials of the various species. If we now relax the constraint of non-reactive mixture and impose the chemical equilibrium for all reactions in Eq. (2), one must have

$$\mu_{i-1} + \mu_1 = \mu_i \quad (3 < i \leq z^*). \quad (5)$$

At the same time, we require that the relevant composition variables, N_t and N_f , are related to species composition variables by

$$N_t = N_1 + 3N_3 + 4N_4 + 5N_5 + \dots + z^* N_{z^*} \quad (6)$$

and

$$N_f = N_3 + N_4 + N_5 + \dots + N_{z^*}. \quad (7)$$

Taking into account Eqs. (5), (6) and (7), Eq. (4) becomes

$$dF = -SdT - p_N AdL - p_T LdA + \mu_1 dN_t + (\mu_3 - 3\mu_1) dN_f. \quad (8)$$

In terms of the adopted independent variables, the normal pressure p_N and the free monomer chemical potential μ_1 are thus formally given by

$$p_N = -\frac{1}{A} \left(\frac{\partial F}{\partial L} \right)_{N_t, N_f, A, T}, \quad (9)$$

$$\mu_1 = \left(\frac{\partial F}{\partial N_t} \right)_{N_f, A, L, T}. \quad (10)$$

By analogy with in vitro experimental conditions where the confined bundle in solution is in thermodynamic and chemical equilibrium with an effective large reservoir of a free monomer solution at the same temperature T and same monomer chemical potential μ_1 , it is useful to identify the pressure exerted by the filament brush on the opposite wall, not by the total pressure p_N defined in Eq. (9), but by the excess (osmotic) pressure Π defined by

$$\Pi = p_N - p^\infty(\mu_1, T) \quad (11)$$

where $p^\infty(\mu_1, T)$ is the isotropic pressure in the reservoir fluid (free monomers) with specific number density $\rho_1^\infty(\mu_1, T)$. The activity coefficient f_1^∞ of this reservoir solution which takes into account all interactions between the free monomers is defined by the expression using the ideal solution as reference state,

$$\begin{aligned} \beta\mu_1 &= -\ln(q_1/V) + \ln(f_1^\infty \rho_1^\infty), \\ &= \ln \Lambda^3 + \ln(f_1^\infty \rho_1^\infty) \end{aligned} \quad (12)$$

where q_1 is the ideal gas single monomer partition function at same temperature T and Λ is the de Broglie wave length associated to the free monomers.

Considering all permanent grafting points as equivalent, we can define the activity coefficient f_i of a grafted filament of size i in the brush/solution system at temperature T as

$$\beta\mu_i = -\ln q_i + \ln(f_i P_i) = -\ln(q_i^0 \alpha_i) + \ln(f_i P_i) \quad (13)$$

where $q_i(T, L)$ is the ideal solution partition function at temperature T of a single chemisorbed filament of size i in interaction (if sufficiently long) with the opposite obstacle wall and where $P_i = N_i/N_f$ is the number fraction of filaments of size i . In the second equality of Eq. (13) we introduce the ideal solution partition function $q_i^0(T)$ for the same grafted filament of size i in absence of the obstacle wall. The wall factor $\alpha_i(L, T)$ is given by

$$\alpha_i = \frac{q_i}{q_i^0} = \langle \exp(-\beta U^w) \rangle_i^0 \quad (14)$$

where $\langle \dots \rangle_i^0$ is a canonical average ($\beta = (k_B T)^{-1}$) based on a single grafted filament Hamiltonian H_i^0 for a filament of size i in absence of wall interaction term U^w . These wall factors are trivially equal to unity as long as the single grafted filament does not hit the opposite wall, which defines an upper limit z for the series of filaments avoiding any direct interaction with the wall which should be of the order $z \approx L/d$.

Combining Eqs. (5), (12) and (13), one gets [19]

$$K_{0i} \equiv \frac{q_i}{q_{i-1} \Lambda^{-3}} = \frac{f_i}{f_{i-1} f_1^\infty} \frac{P_i}{P_{i-1} \rho_1^\infty}, \quad (15)$$

where we introduce the equilibrium constant K_{0i} of the reaction in Eq. (2) within the reference ideal system, a quantity depending only on the temperature (and possibly L). In terms of wall factors, the ideal solution equilibrium constant can be reformulated as

$$K_{0i} = \frac{q_i^0}{q_{i-1}^0 \Lambda^{-3}} \frac{\alpha_i}{\alpha_{i-1}} = K_0 \frac{\alpha_i}{\alpha_{i-1}} \quad (16)$$

where we have assumed [1] that the (de)polymerizing equilibrium constant of the active free end of the filament in bulk, noted K_0 , is independent of the filament size.

Finally, the special form of the chemical potential Eq. (13) which disentangles wall and interaction effects, lead to filament populations satisfying a set of equalities

$$\frac{P_i}{P_{i-1}} = \rho_1^\infty K_0 \frac{\alpha_i}{\alpha_{i-1}} \frac{f_{i-1} f_1^\infty}{f_i} \quad (3 < i \leq z^*) \quad (17)$$

For the ideal bundle case, these relations take the form

$$\frac{P_i^{\text{id}}}{P_{i-1}^{\text{id}}} = \rho_1 K_0 \frac{\alpha_i}{\alpha_{i-1}} \quad (3 < i \leq z^*) \quad (18)$$

where ρ_1 is the free monomer density.

B. The ideal bundle properties

The statistical mechanics properties of the ideal bundle case in the (N_t, N_f, A, L, T) canonical reactive ensemble was treated in detail elsewhere. [17] In terms of the reduced equilibrium free monomer density $\hat{\rho}_1 = \rho_1 K_0$, the filament number fractions in the ideal solution at equilibrium are given by

$$P_i^{\text{id}} = \frac{N_i}{N_f} = \frac{(\hat{\rho}_1)^i}{D} \quad (3 \leq i \leq z), \quad (19)$$

$$P_{z+k}^{\text{id}} = \frac{N_{z+k}}{N_f} = \alpha_{z+k}(L) \frac{(\hat{\rho}_1)^{z+k}}{D} \quad (1 \leq k \leq k^*), \quad (20)$$

where the normalization factor is given by

$$D = \left[\sum_{i=3}^z (\hat{\rho}_1)^i \right] + \sum_{k=1}^{k^*} \alpha_{z+k}(L) (\hat{\rho}_1)^{z+k}. \quad (21)$$

Equation (19), valid for filaments too short to interact with the wall, is an exponential size distribution $\propto \exp(i/s)$ with $s = [\ln \hat{\rho}_1]^{-1}$, where $|s|$ is the characteristic length scale (in monomer units) of the growing ($\hat{\rho}_1 > 1$) or decreasing ($\hat{\rho}_1 < 1$) exponential distribution. Equation (20) deals with filaments of size $z + k$ hitting the wall, where k is limited by $k^* = z^* - z$. Equations (19) and (20) are compatible with Eq. (18). To express this filament distribution in terms of the original independent variables of the reactive canonical ensemble, one substitutes the filament densities Eqs. (19) and (20) in the constraint relationship Eq. (6) and gets the ρ_1 implicit equation

$$\rho_t = \rho_1 + \frac{\sigma_f}{L} \langle i \rangle = \rho_1 + \frac{\sigma_f}{L} \frac{M(\hat{\rho}_1, L)}{D(\hat{\rho}_1, L)}, \quad (22)$$

where ρ_t is the total monomer number density, σ_f is the filament surface density and $\langle i \rangle$ is the average length of the filaments in the bundle. In Eq. (22), D is given by Eq. (21) and $M = \hat{\rho}_1 \partial D / \partial \hat{\rho}_1$.

In Ref., [17] by applying Eq. (9) to the theoretical expression of the free energy of the ideal bundle solution, we get the normal pressure p_N on the obstacle wall as

$$\beta p_N = \rho_1 + \sigma_f \left(\frac{\partial \ln D}{\partial L} \right)_{\hat{\rho}_1}. \quad (23)$$

Using Eq. (11) with $p^* = \rho_1 k_B T$, one gets the force per filament f_N^{id} in an ideal solution as

$$\beta f_N^{\text{id}} = \frac{\Pi}{\sigma_f k_B T} = \left(\frac{\partial \ln D}{\partial L} \right)_{\hat{\rho}_1} = \sum_{k=1}^{k^*} \beta \bar{f}_{z+k} P_{z+k}^{\text{id}}. \quad (24)$$

In Eq. (24), the new force \bar{f}_{z+k} appearing in the last term derives from a potential of mean force

$$w_{z+k}(L) \equiv -k_B T \ln(\alpha_{z+k}(L)), \quad (25)$$

and thus represents the force exerted by the wall on a filament of fixed contour length $z + k$, averaged over all the microscopic degrees of freedom associated to its single grafted filament Hamiltonian H_{z+k} . According to Eq. (24), the equilibrium normal force f_N^{id} is the weighted average of the force \bar{f}_{z+k} , using absolute probabilities given by Eq. (20), over all hitting filament species denoted by $k = 1, k^*$. The chemical conditions are fixed by $\hat{\rho}_1$, while all structural aspects including the persistence length and the precise nature of the repulsive wall potential U^{ext} are absorbed in the L dependence of the different $\alpha_{z+k}(L)$ wall factors given by Eq. (14). This is equally true for p_N in Eq. (23), which represents the force per unit area originating from independent living filaments defined by the same specifications. These wall factors, which are responsible for the size distribution of grafted living filaments hitting a wall perpendicular to their initial grafting orientation, have been shown [18] to present universal relations for the model of a continuous wormlike chain (WLC) model hitting a hard wall, as long as $L/l_p < 0.1$. The explicit universal relations express $\alpha \equiv \tilde{Z}(\tilde{\eta})$ in terms of the rescaled compression variable

$$\tilde{\eta} = \frac{L_c - L}{L_{\parallel}} = \frac{(L_c - L)l_p}{L_c^2} \quad (26)$$

where L_c is the contour length of the filament and L_{\parallel} a characteristic length. For other filament/wall models or for more flexible WLC, the derivation of the wall factors require Monte-Carlo calculations, as discussed in references. [17, 18]

The theoretical developments of this work require that filaments are sufficiently rigid over the gap size L to prevent filaments to grow laterally. This was formulated by requiring that the thermodynamic conditions guarantee that $P_{z^*} \cong 0$, where z^* is given by Eq. (3). Guided by the ideal bundle results and the universal properties of the wall factor, [18] it can be shown [17] that if $L/l_p < 0.1$, the reduced density must remain below a limit value ρ_{1b} , namely

$$\ln \hat{\rho}_1 < \frac{l_p d}{L^2} \equiv \ln \hat{\rho}_{1b}. \quad (27)$$

This point was also carefully discussed in Ref. [4] dealing with the measurement of the compressive force of a bundle of stiff actin filaments. The data exploited in that study were obtained in conditions where Eq. (27) applies.

III. THE SPECIFIC MODEL WITH INTERMOLECULAR INTERACTIONS FOR THE CONFINED SELF-ASSEMBLING GRAFTED BUNDLE

A. Model Hamiltonian for a grafted and confined single filament and single living filament properties

Let us first describe the basic ingredients of the model, namely the way a filament of size N is built as a linear assembly of N point particles of mass m with Cartesian coordinates $\{\mathbf{r}_i\}$ and momenta $\{\mathbf{p}_i\}$ with $i = 1, \dots, N$. To

graft the filament to the $x = 0$ plane, the two first monomers are fixed in space by two independent infinitely stiff springs to positions ($\mathbf{r}_1 \equiv (0, y_\gamma, z_\gamma)$, $\mathbf{r}_2 \equiv (d, y_\gamma, z_\gamma)$) defining the first rigid bond of length d of the filament at location γ of the grafting surface, with normal orientation with respect the latter. The adopted single filament Hamiltonian is

$$\begin{aligned} H_N(\mathbf{r}, \mathbf{p}) &= \sum_{i=1}^N \frac{\mathbf{p}_i^2}{2m} - (N-1)\epsilon'_0 + \sum_{i=2}^{N-1} \frac{k_s}{2} (d_i - d)^2 \\ &+ \frac{\kappa}{d} \sum_{i=2}^{N-1} (1 - \cos \theta_i) + \frac{N-2}{2\beta} \ln \frac{2\pi}{\beta k_s d^2} \\ &+ U_N^{\text{ext}}, \end{aligned} \quad (28)$$

which starts with the kinetic energy term. The second term expresses the bonding energy corresponding to the energy released as heat when a new monomer attaches the filament and forms a new bond. There are $N - 2$ bonds $\mathbf{d}_i = \mathbf{r}_{i+1} - \mathbf{r}_i$ of (almost) constant length d (the first bond length is automatically fixed by the grafting conditions) as we consider in the third term stiff harmonic springs with d_i supposed to oscillate harmonically around d . The next term accounts for the bending energy where θ_i is the bending angle between bonds \mathbf{d}_{i-1} and d_i , while the bending modulus κ fixes the persistence length l_p of the filament according to $\kappa = k_B T l_p$. Our interest lies in situations where $l_p \gg L$.

The constant fifth term is useful to normalize the $\exp(-\beta k_s (d_i - d)^2 / 2)$ term which will appear in the filament canonical partition function (or in any phase space integral) in order to allow the (scalar) Gaussian bond length distribution around the mean d to properly evolve towards the delta function in the $k_s \rightarrow \infty$ limit (harmonic bond stiff limit). In Ref. [16] the Hamiltonian was defined without the fifth normalizing term now appearing in Eq. (28). For consistency, the bonding energy ϵ_0 in Ref. [16] must then be linked to the present bonding energy parameter using [17]

$$\beta \epsilon'_0 = \beta \epsilon_0 + \frac{1}{2} \ln \left(\frac{2\pi}{\beta k_s d^2} \right). \quad (29)$$

The external potential term which controls the interaction of the filament with the obstacle wall is represented as $U_N^{\text{ext}} = \sum_{i=3}^N U^w(L - x_i)$, where among all monomer-wall interactions, only terms with distance to the wall within the cut-off distance x_c ($L - x_i < x_c$) contribute. We adopt the specific form

$$U^w(s) = \frac{3\sqrt{3}}{2} \epsilon_w \left[\left(\frac{\sigma_w}{s} \right)^9 - \left(\frac{\sigma_w}{s} \right)^3 \right] + \epsilon_w, \quad (30)$$

where $s = L - x$ is the distance between a monomer center and the wall. The cutoff distance is chosen at the minimum of the potential, hence $x_c = 3^{1/6} \sigma_w$.

In Eq. (13), we introduced two forms of the canonical partition function at temperature T of a single filament of size $3 \leq i \leq z^*$ grafted to one wall, namely $q_i(L, T)$ and $q_i^0(T)$ to be distinguished respectively by the inclusion or not of confining opposite wall U^w terms. These partition functions, now fully determined by the single filament Hamiltonian Eq. (28) including the wall potential, Eq. (30), can be exploited to compute two relevant quantities needed to establish the link between our non-ideal simulations with the ideal bundle case. Using Eq. (14), the wall factors $\alpha_i(L, T)$ can be determined by Monte-Carlo sampling [17]. Next, according to Eq. (16), the equilibrium constant K_0 of the (de)polymerization reaction Eq. (2) in absence of wall interference can be established and one gets, as expected, an i -independent equilibrium constant [17]

$$K_0 = \frac{q_i^0}{q_{i-1}^0} \Lambda^3 = \frac{2\pi d^4}{l_p} \exp(\beta \epsilon'_0) [1 - \exp(-2l_p/d)] F(w_0) \quad (31)$$

where the last term is a correcting factor for the bond flexibility function of $w_0 = d/\sigma_d = \sqrt{\beta k_s d^2}$ which is explicitly given by

$$F(w_0) = \frac{\frac{1+\text{erf}[w_0]}{2}(1+w_0^2) + \frac{w_0}{\sqrt{2\pi}} \exp(-\frac{w_0^2}{2})}{w_0^2}, \quad (32)$$

where the error function erf is used. In the stiff bond limit (discrete WLC model), one trivially observes that $\lim_{k_s \rightarrow \infty} F(w_0) = 1$.

B. Model Hamiltonian for a bundle of self-assembled filaments and free monomers in interaction and the corresponding reactive canonical ensemble

We will specifically perform Molecular Dynamics simulations with explicit chemical steps in order to probe the reactive canonical partition function $Q^{\text{RC}}(N_t, N_f, A, L, T)$ relative to a bundle of N_f grafted filaments of variable length confined in a slit pore of gap width L and transverse square area $A = H^2$, in thermal contact with a thermostat at temperature T . The N_f filaments are grafted at the vertices, denoted by index $\gamma = (1, N_f)$, of a centered square lattice with unit cell length a adjusted to get a predefined surface density $\sigma_f = N_f/H^2 = 2/a^2$. The pore encloses in total N_t monomers which can either be independent free monomers or integrated within a grafted self-assembled filament.

The partition function Q^{RC} is a sum of standard canonical partition functions over all distinguishable ways to group the N_t monomers into topologies satisfying the global constraints Eqs. (6) and (7), where to each chemisorption site γ is associated a specific filament size $i(\gamma)$ in the allowed range ($3 \leq i(\gamma) \leq z^*$) while all remaining monomers are treated as free monomers (the explicit form of Q^{RC} is mentioned in Appendix A). To each topology is associated an Hamiltonian H^{tot} and corresponding canonical ensemble partition function. This Hamiltonian can be formally written as the sum of all single filament Hamiltonians H_N (Eq. (28) with $N = i(\gamma)$ for any site γ) and all single free monomer Hamiltonian h_k

$$h_k = \left[\frac{\mathbf{p}_k^2}{2m} + U^{\text{w}}(x_k) + U^{\text{w}}(L - x_k) \right] \quad (33)$$

grouping kinetic and wall interaction potentials, to which intermolecular interactions must be added. One thus gets

$$H^{\text{tot}} = \sum_{\gamma=1}^{N_f} H_{i(\gamma)} + \sum_{k=1}^{N_1} h_k + U^{\text{ev}} \quad (34)$$

where $N_1 = N_t - \sum_{\gamma=1}^{N_f} i(\gamma)$ and where the excluded volume interactions term U^{ev} is taken as in our previous study, [16] as the sum of purely repulsive interactions (Weeks-Chandler-Andersen (WCA) potential) between all pairs of monomers except between pairs of monomers belonging to the same filament.

The exploration of the full reactive ensemble is performed during the Molecular Dynamics trajectory by performing in addition (according to stochastic rules) topological changes through explicit polymerization steps (when a free monomer is close to a filament free end) or through depolymerization steps. The rules were defined in Ref. [16] and are trivially adjusted for the present study by adding the wall potential terms to the excluded volume potential terms for the reacting monomer in the Monte-Carlo chemical step procedure. Consequently, a depolymerization step where the freed monomer is relocated at a place of too high wall potential energy, will typically be refused. Also, for the polymerization step, the availability of free monomers in the reactive volume (close to the tip of the receiving filament) to attempt a polymerization step will be lowered by the wall presence when the filament tip precisely hits the wall.

C. Computer simulation experiments: Choice of parameters and list of experiments

A bundle of $N_f = 32$ filaments is grafted at one wall of square area $A = H^2$, the filaments seeds being permanently linked to the sites of a centered square lattice of unit cell size $H/4$. A free monomer solution fills the gap of width L between the grafting plane and the obstacle parallel plane while periodic boundary conditions are used in transverse directions, giving rise to a slit pore confining volume $V = AL$. The hybrid Molecular Dynamics - Multiparticle Collision Dynamics - Monte-Carlo (MD-MPCD-MC) method follows dynamically the system of N_t monomers according to the Hamiltonian, Eq. (34), and performs in addition local (de)polymerization steps, thus sampling the reactive canonical ensemble associated to our system at fixed (N_t, N_f, A, L, T) . The solute system of N_t monomers is coupled to a MPCD bath, the temperature being explicitly fixed by its value in the acceptance rules of the Monte-Carlo chemical steps. [16] The side a_0 of the elementary MPCD (local) collisional cubic boxes is taken as twice the monomer size increment d of the filaments. [16] The simulation box has its L and H dimensions corresponding to an integer number of a_0 , all experiments having been performed for the same gap width $L = 8a_0 = 16d$. Table I summarizes the specific parameters of the different series of experiments denoted by roman numbers I-III ordered by increasing filament brush surface densities but differing also by the choice of the ideal solution equilibrium constant K_0 . Experiments I and IIb adopt the same K_0 value, while this constant is halved for experiment IIa and again halved for experiment III. Each of the four series of experiments are performed for several values for the total number of monomers, N_t to cover various sub- and supercritical regimes.

TABLE I. List of simulation experiments performed at $k_B T = 1$, $L = 16d$, $l_p = 250d$ and $\nu = 50u_t^{-1}$, regrouped into four experiment series in which only the total number of monomers N_t is changing. The transverse area is $A = H^2$, the brush surface density is $\sigma_f = N_f/A$, the equilibrium constant K_0 (see Eq. (31)) is based on different values of ϵ'_0 , namely 8.04211 (I, IIb), 7.34894 (IIa) and 6.61497 (III).

Experiment	H/d	N_f	N_t	$\sigma_f d^2$	K_0/d^3
I	16	32	450, 500, 525 550, 600	0.1250	78.1397
IIa	12	32	230, 300, 370 437, 500, 550	0.2222	39.0698
IIb	12	32	371, 438 501, 551	0.2222	78.1397
III	10	32	240, 290, 350 430, 490, 540	0.3200	18.7535

We now list the parameters adopted in our simulations using $k_B T$ as energy unit, the MPCD solvent mass m_s as unit of mass, and finally a_0 as unit of length. The time unit is $u_t = a_0 \sqrt{m_s/k_B T}$. The monomers (either free or part of the filaments) have a mass $m = 5m_s$. The bond length at potential minimum $d = 0.5a_0$ will also be regularly used when mentioning results in reduced variables implying length scales. The bonding force constant is taken to be $k_s = 400k_B T/d^2$. The bending potential is fixed by $l_p/d = 250$, with $\kappa = k_B T l_p/d$. The bonding energy parameter ϵ'_0 varies for the different sets of experiments (see Table I). For experiment IIa, we take $\epsilon'_0 = 7.34894$, which gives $K_0 = 4.88373a_0^3$ according to Eq. (31) (note that this set of parameters is fully equivalent to the one used in the previous work where we took $\epsilon_0 = 9.42573$ in Eq. (31) in Ref. [16].) The Lennard-Jones (LJ) parameters for the WCA pair interaction is set to $\sigma = 0.44545a_0$ and $\epsilon = 3k_B T$, while for the wall potential U^w in Eq. (30) the two parameters were set to $\sigma_w = 0.5a_0 = d$ and $\epsilon_w = 0.1k_B T$ and the cutoff distance (chosen at minimum of potential) is $x_c = 3^{1/6}\sigma_w = 1.200936d$. The MPCD parameters are the solvent density $\rho_s = 5a_0^{-3}$, the collision time interval $\Delta t = 0.1u_t$, and the collision rotation angle of $\alpha = 130$ degrees. The equations of motion for solute filaments and free monomers are integrated using the velocity version of the Verlet algorithm with MD time step of $h = 0.002u_t$. The last parameter to be fixed is the attempt frequency ν with which any reactive monomer (polymerizing or depolymerizing) is subject to an attempted chemical step, the central parameter controlling the time scale on which the filament contour length dynamics takes place. [16] With respect to our previous work, we took $\nu = 50u_t^{-1}$ instead of 5 to accelerate the establishment of chemical equilibrium.

IV. SIMULATION RESULTS

Simulation data were obtained, for each state point investigated, by averaging over four independent MD-MPCD-MC runs of $T_{\text{run}} = 10^5 u_t$ which represents one order of magnitude longer than the single filament contour length relaxation time τ_i (see Table II).

Each run was preceded by an equilibration run of $T_{\text{run}} = 10^4 u_t$ starting with N_f filament seeds of three units attached to the left wall (given our choice of three beads filaments as effective seeds, see Eq. (2)) and a set of $N_t - 3N_f$ free monomers disposed at 3D cubic lattice vertices, to optimize initial space homogeneity of the monomer density. Note that in preparing the equilibrium trajectory of any bundle+free monomers solution state point by a preliminary explicit growth of the bundle from a non-equilibrium initial configuration with filament seeds and free monomers only, we automatically tested the robustness of our simulation scheme in reproducing in a systematic way the studied network equilibrium state.

The results of the three series of experiments I, II (including IIa and IIb) and III ordered by increasing grafting density, are gathered in Tables III, IV and V respectively. Within each table, the data are organized such that the total number N_t of monomers in the system increases from top to bottom, so that the system evolves typically from a subcritical regime up to more and more supercritical regimes (note that in experiment series I and IIb, only supercritical regimes are considered).

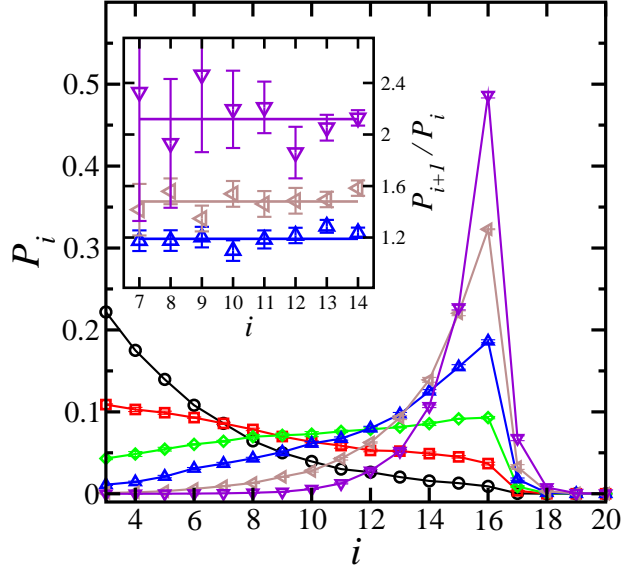


FIG. 2. Distribution of filament sizes obtained in the simulation series IIa of experiments at surface density $\sigma_f d^2 = 0.222$ for N_t values 230 (circles), 300 (squares), 370 (lozenges), 437 (triangles pointing up), 500 (triangles pointing left) and 550 (triangles pointing down). Continuous lines have been drawn for better data visualization. Inset: the ratios P_{i+1}/P_i are plotted versus i (for $i < z$) for the experiments $N_t = 437, 500, 550$ to which corresponds, in the same order, an increasing $\hat{\rho}_1^{\text{eff}}$ fitting value indicated by an horizontal line (see text).

A. Distribution of filament lengths and free monomer distribution

Figures 2 and 3 show respectively the distributions of filament sizes and the corresponding free monomer densities averaged along the transverse directions, for the various state points considered at intermediate density $\sigma_f d^2 = 0.222$.

We observe in Fig. 2, that all distributions are reasonably smooth up to $i = 16$ (inclusive). This is coherent with an independent filament Monte-Carlo prediction of the wall factors defined by Eq. (14), using the Hamiltonian H_N given by Eq. (28) with parameters taken identical to those adopted in our MD simulations. Given the slightly flexible bonds with fluctuations ($\sigma_d/d = 0.05$) and the range of the wall potential ($x_c/d \cong 1.20$), the index of the largest filament which has essentially no direct interactions with the wall is $z = 15$. The α_{z+k} were obtained by a Metropolis MC sampling of an anchored filament of size $z = 15$ to which up to six extra bonds are added to probe the wall potential energy Boltzmann factor. [17] We get $\alpha_{16} = 0.9245(4)$, $\alpha_{17} = 0.11700(2)$, $\alpha_{18} = 0.01400(4)$, $\alpha_{19} = 0.0026(1)$, $\alpha_{20} = 0.00069(6)$ and $\alpha_{21} = 0.00024(2)$, indicating a weak wall perturbation for $i = 16$ and a strong wall perturbation for larger sizes. According to Eq. (20), the size distribution in the ideal case will show a clear drop for $i \geq 17$, and this is observed in our MD results also.

The free monomer density $\rho_1(x)$ is now a field variable and we observe that it is correlated to the co-volume of the filaments which follow a size exponential distribution shown in Fig. 2. Among the six systems considered at the same temperature and same surface density, the first system is clearly subcritical (apparent exponential decay of filament size populations) while the three last cases are supercritical (apparent exponential increase of filament size populations before wall influence). The second and third systems are close to the critical regime with a slight sub- or supercritical character respectively.

We found that the size distributions for $i \leq z = 15$ are all very well described by an exponential function,

$$P_i \propto \exp [\ln (\hat{\rho}_1^{\text{eff}}) i], \quad (35)$$

implying according to Eq. (17)

$$P_i/P_{i-1} = \rho_1^\infty f_1^\infty \frac{f_{i-1}}{f_i} K_0 \approx \hat{\rho}_1^{\text{eff}}. \quad (36)$$

Eq. (36), verified in the inset of Fig. 2, suggests that the ratio $r_i = f_{i-1}/f_i$ is effectively independent of the filament size. In Tables III, IV and V are reported all estimates of the effective free monomer density $\hat{\rho}_1^{\text{eff}}$, a quantity which turns out to provide a measure of the degree of supercriticality of a particular state point and which reduces naturally

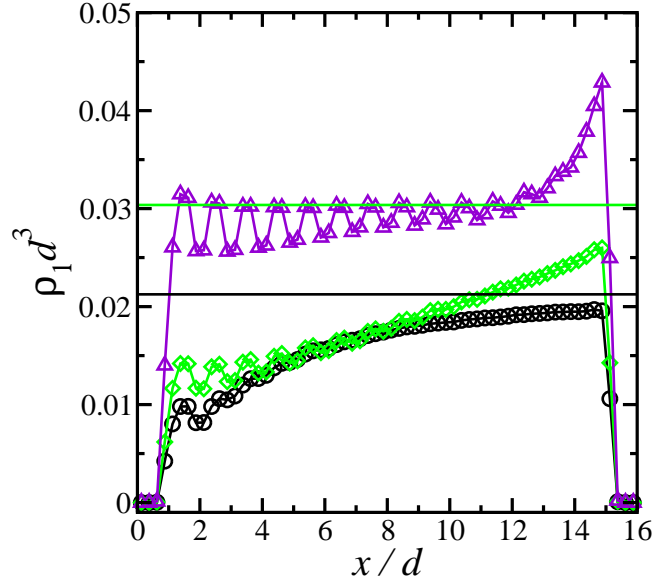


FIG. 3. Free monomer density as a function of x/d from the anchoring wall at ($x=0$) to the obstacle wall at ($x/d=16$) in the simulation series IIa of experiments at surface density $\sigma_f d^2 = 0.2222$, for N_t values 230 (black circles), 370 (green lozenges), 550 (violet triangles). Corresponding values of ρ_1^∞ are indicated as a continuous horizontal line of same color except for the highest density $\rho_1^\infty d^3 = 0.0725$ (for $N_t = 550$) lying outside the shown density window.

to $\hat{\rho}_1 = K_0 \rho_1$ in the ideal case when all activity coefficients are unity and ρ_1^∞ becomes equivalent to the uniform ρ_1 value.

As a digression, we now discuss some preliminary data of experiment IIa listed separately in Table II. They provide a general structural and dynamical information which helps appreciating some general trends as N_t increases and also allows us to verify that simulation averages deal with well equilibrated systems. With ρ_t increasing, the average size of filaments and the correlated average height (end-to-end vector projected onto x) of the brush systematically increases. As could be expected, the amplitude of the size fluctuations and their characteristic relaxation time τ_i are largest close to the critical regime ($\hat{\rho}_1^{\text{eff}} = 1$). We note that the sampling time window of each of the four independent MD runs per experiment (whose averages are provided in tables) is at least a factor ten larger than the intrinsic relaxation time τ_i . This explains our choice to adopt a larger value of the ν parameter with respect to our first study in Ref. [16] The averaged (de)polymerization rates $\langle U \rangle$ and $\langle W \rangle$ per filament-end in Table II are averages over all filament sizes. The same frequency observed for polymerization and depolymerization events is an additional indication of equilibrium. As ρ_t increases, one first observes an increase of the chemical events frequency as a result of the increase of the free monomer density and in parallel, an increase of the fraction of filaments able to depolymerize ($i \geq 4$). As ρ_t further increases, the overall rates start decreasing because the wall presence forbids easy polymerization of the most populated long filaments and at the same time the relatively high packing fraction causes a decrease of the acceptance rate of the attempted chemical events. [16]

B. Data on normal pressure/compressive force and free monomers chemical potential

The force exerted by a monomer i located at a close distance x from the right wall, with $x = x_{\text{wr}} - x_i < x_c$ where x_c is the wall interaction cutoff distance, exerts on the wall a positive force deriving from Eq. (30)

$$f(x) = \frac{9\sqrt{3}}{2} \epsilon_w \left[3 \left(\frac{\sigma_w}{x} \right)^9 - \left(\frac{\sigma_w}{x} \right)^3 \right] \frac{1}{x}. \quad (37)$$

The pressure on the right wall can be estimated directly as

$$p_N = p_w^s + p_w^{\text{fm}} + p_w^{\text{br}} \quad (38)$$

where p_w^s originates from average normal linear momentum exchange per unit area due to solvent (MPCD) particles reflections. The free monomer contribution p_w^{fm} and the filament contribution p_w^{br} are the average of the sum per unit

TABLE II. Equilibrium data on a brush of $N_f = 32$ filaments pressing against a fixed wall at density $\sigma_f d^2 = 0.2222$ (Experiment IIa with $K_0 d^{-3} = 39.0698$). N_t is the total number of monomers in the volume $V/d^3 = 2304$ which also contains 1440 MPCD solvent particles. $\langle i \rangle$ is the average size of a filament expressed in the number of monomers, including those which initiate the filament at the left wall. The two next columns provide data on the filament size fluctuations, namely their amplitude and characteristic relaxation time τ_i . $\langle X_i \rangle$ is the averaged projection of the end-to-end vector of the filaments on the normal to the walls (x axis). $\langle U \rangle$ and $\langle W \rangle$ are the average (de)polymerization rates per free filament end. Note that times and frequencies are made dimensionless by using the time unit u_t defined in Sec. III C and unmentioned errors are of one unit on the last digit indicated.

N_t	$\langle i \rangle$	$\langle \delta i^2 \rangle^{1/2}$	$\tau_i / (10^3 u_t)$	$\langle X_i / d \rangle$	$\langle U u_t \rangle$	$\langle W u_t \rangle$
230	6.16	3.16	5.6	5.12 (1)	0.00208	0.00208
300	8.26	3.91	8.2	7.17 (1)	0.00236	0.00236
370	10.39	3.94	7.9	9.26 (1)	0.00241	0.00241
437	12.41	3.41	7.3	11.20 (1)	0.00233	0.00233
500	14.17	2.32	4.0	12.92 (2)	0.00214	0.00215
550	15.24	1.38	1.4	13.93 (2)	0.00187	0.00187

area of all contributions of the type in Eq. (37) coming respectively from free monomers and from filament monomers. This wall normal pressure (computed at the wall) is equivalent at equilibrium to the xx -component of the pressure tensor computed at any point in the system. We did check this property by computing $p_{xx}(x)$ as a sum of all linear momentum transfers per unit area across a virtual surface normal to x -axis at equally spaced values in the range $0 < x < L$. We found that wall pressure p_N data and volume average of the p_{xx} values lead to same estimates of the homogeneous normal pressure (within error bars) and the statistical accuracy is similar.

The free monomer chemical potential was computed according to a Widom-like virtual particle expression derived in Supplementary Material, A for the reactive canonical ensemble, which can be summarized as follows:

$$\beta\mu_1 \equiv \ln \frac{\Lambda^3}{d^3} + \beta\mu_1^*, \quad (39)$$

$$\begin{aligned} \beta\mu_1^* &= -\ln \left[\frac{V}{d^3} \left\langle \frac{1}{(N_1 + 1)} \int_0^1 ds_{\text{ex}}^3 \exp[-\beta\Delta U_{\text{ex}}] \right\rangle \right], \\ &= -\ln \left[\frac{V}{d^3} \left\langle \frac{E}{(N_1 + 1)} \right\rangle \right], \end{aligned} \quad (40)$$

where $\langle \dots \rangle$ represents a reactive canonical ensemble average. Within the averaged quantity, N_1 is the instantaneous number of free monomers in the microscopic configuration and E represents the triple integral over s_{ex} which must be estimated, for a given microscopic configuration of the system, by a distinct MC sampling of three independent random numbers s_x, s_y and s_z in an homogeneous distribution $[0, 1]$. As indicated in Eq. (40), E requires the average of the exponential factor of the additional potential energy ΔU_{ex} due to the interactions between an extra virtual particle located at random location $x = s_x L, y = s_y H$ and $z = s_z H$ and both the wall and the N_t monomers of the system.

In Tables III, IV and V, we report for all three series of experiments the averaged wall pressure contributions p_w^{fm} and p_w^{br} defined in Eq. (38) and the estimates of the average of $\langle E / (N_1 + 1) \rangle$ and corresponding values of $\beta\mu_1^*$, according to Eq. (40). The estimate of $\langle E / (N_1 + 1) \rangle$ is based on 200 independent extra particle insertions for each treated microscopic configuration, the latter being those saved along the trajectory at equally spaced time intervals of $100u_t$ (so a total of 4×10^3 configurations per experiment).

In the following, we need to know the thermodynamic properties of the free monomer solution which would be in equilibrium with the simulated bundle/free monomers system and we will denote these reservoir equilibrium properties, as already done in Sec. II, with an ∞ superscript. We checked that the virial expansion of the pressure p^∞ and the chemical potential μ_1^{∞} up to the second virial coefficient is sufficiently precise for the relevant concentration regime,

TABLE III. Equilibrium data on a brush of $N_f = 32$ filaments pressing against a fixed wall at density $\sigma_f d^2 = 0.125$ (Experiment I). N_t is the total number of monomers in the volume $V/d^3 = 4096$ which also contains 2560 MPCD solvent particles. $\langle \rho_1 \rangle$ is the average free monomer density in the total volume V . The quantity $\langle E/(N_1 + 1) \rangle$ is the average expression in the argument of the logarithm term used in Widom-like formula Eq. (40), which then leads to $\beta\mu_1^*$ reported in next column. The two next columns provide the reduced free monomer concentration defined as $\hat{\rho}_1 = \exp(\beta\mu_1^*)K_0$ (with $K_0/d^3 = 78.13968$ in the present case) and the effective density $\hat{\rho}_1^{\text{eff}}$ obtained by an exponential fitting of the P_i simulation data. The next column provides an estimate of the apparently i independent ratio $r = f_{i-1}/f_i$ evaluated as the ratio $\hat{\rho}_1^{\text{eff}}/\hat{\rho}_1$. p_w^{br} and p_w^{fm} are respectively the contributions of the brush and the free monomers to the pressure exerted on the right wall, p^∞ is the pressure in the pure monomer solution in chemical equilibrium with the brush. The last column provides the reduced force per filament computed as $f_N = (p_w^{\text{br}} + p_w^{\text{fm}} - p^\infty)\sigma_f^{-1}$. Note that the limit for buckling for an independent filament is $\hat{\rho}_1^{\text{b}} = \exp(l_p d/L^2) = 2.66$, so that the $N = 600$ case needs to be considered with care as the effective $\hat{\rho}_1^{\text{eff}} = 2.6 \cong \hat{\rho}_1^{\text{b}}$.

N_t	$\langle \rho_1 d^3 \rangle$	$\langle E/(N_1 + 1) \rangle$	$\beta\mu_1^*$	$\hat{\rho}_1$	$\hat{\rho}_1^{\text{eff}}$	r	$\beta p_w^{\text{br}} d^3$	$\beta p_w^{\text{fm}} d^3$	$\beta p^\infty d^3$	$\beta f_N d$
450	0.01109(3)	0.0140(1)	-4.049(7)	1.36(1)	1.21(1)	0.89(2)	0.0261(7)	0.0157(1)	0.01689	0.200(6)
500	0.0125(3)	0.0119(1)	-3.887(8)	1.60(1)	1.46(1)	0.91(2)	0.0439(6)	0.0182(4)	0.01989	0.338(6)
525	0.0141(2)	0.01025(8)	-3.737(8)	1.86(1)	1.59(1)	0.85(2)	0.0597(6)	0.0206(4)	0.02292	0.459(6)
550	0.0164(2)	0.00862(6)	-3.564(7)	2.21(2)	1.86(1)	0.84(2)	0.073(1)	0.0235(1)	0.02705	0.557(8)
600	0.0227(1)	0.00591(3)	-3.187(5)	3.23(2)	2.64(1)	0.82(2)	0.116(3)	0.0320(3)	0.03875	0.87(2)

and so we used

$$\frac{p^\infty}{k_B T} \cong \rho_1^\infty (1 + B_2 \rho_1^\infty), \quad (41)$$

$$\beta\mu_1^{*\infty} \cong \ln(\rho_1^\infty d^3) + 2B_2 \rho_1^\infty, \quad (42)$$

where $B_2/d^3 = 1.722824$ at $k_B T^\infty = 1$, assuming the shifted LJ potential with cutoff at minimum (see Sec. III C or see Eq. (2) in Ref. [16]). Imposing $T^\infty = T$ and $\mu_1^{*\infty} = \mu_1^*(N_t, N_f, A, L, T)$ where μ_1^* is known from Eq. (39), we get from Eqs. (41) and (42) the pressure and density of the free monomer fluid reservoir.

Using the second equality of Eq. (36), the i independent ratio $r = f_{i-1}/f_i$ can be estimated from the reduced density $\hat{\rho}_1^{\text{eff}}$ (as reported in Tables) while the free monomer chemical potential μ_1^* is obtained using the connection $d^3 \rho_1^\infty f_1^\infty = \exp(\beta\mu_1^*)$ which follows from Eqs. (10) and (39).

For the evaluation of the osmotic pressure Π in Eq. (11), we need to subtract from p_N the common solvent pressure and the pressure $p^\infty(\mu_1^*, T)$ evaluated by combining Eqs. (41) and (42). The average normal compressive force per filament follows as $f_N = \pi/\sigma_f$, as reported in Tables III, IV and V. Concerning the free monomer density, the same Tables mention the space averaged value $\langle \rho_1 \rangle$ within the bundle which is systematically smaller than the free monomer density ρ_1^∞ of the reservoir solution in equilibrium with it. In Fig. 3, for each state point shown, we indicate by an horizontal line the ρ_1^∞ value corresponding to the $\rho_1(x)$ profile.

In Fig. 4, we plot f_N as a function of $\hat{\rho}_1 = K_0 \rho_1^\infty f_1^\infty$ that we compare with the ideal solution prediction f_N^{id} plotted against $\hat{\rho}_1 = \rho_1 K_0$. The data f_N^{id} were computed according to Eq. (24) using distributions (19,20,21) for $L/d = 16$, $z = 15$ and $k_B T = 1$ on the basis of the α 's and their L derivatives obtained by the single filament Monte-Carlo simulations [17] already discussed in Sec. IV A.

Experiments I and IIb, which have the same ideal solution chemical equilibrium constant, present for the same reservoir free monomers state point, i.e. at the same $\hat{\rho}_1$ value, a weak but systematic decrease of the force f_N with increasing density. If we compare the force f_N between experiments IIa and IIb which correspond to the same grafting density while K_0 is twice larger in the IIb case, we observe that for the same $\hat{\rho}_1$ which corresponds to a much lower free monomer density ρ_1^∞ in IIb (would be twice smaller if system was ideal), the force is significantly larger in IIb than in IIa. If we now compare results of experiments I, IIa and III in that sequence, the points are shifted more and more away from the single independent filament prediction, as an increasing grafting density and a decreasing equilibrium constant K_0 tend both to a reduction of the force.

In Fig. 5, we plot the same values of f_N as a function of $\hat{\rho}_1^{\text{eff}} = \hat{\rho}_1 r = K_0 \rho_1^\infty f_1^\infty f_{i-1}/f_i$ and observe that all points align along the same ideal solution curve given by Eq. (24) already shown in Fig. 4. This is the central result of this paper as it shows that the osmotic force per filament

$$f_N(N_t, N_f, A, L, T) = \phi(L, T, \hat{\rho}_1^{\text{eff}}) \quad (43)$$

TABLE IV. Equilibrium data on a brush of $N_f = 32$ filaments pressing against a fixed wall at density $\sigma_f d^2 = 0.2222$ (Experiment II). The first set of data coined as experiment IIa and the second set of data coined as experiment IIb differ only by a different choice of ϵ'_0 (see Table I) leading to different K_0 values indicated in the extra second column. N_t is the total number of monomers in the volume $V/d^3 = 2304$ which also contains 1440 MPCD solvent particles. See caption of similar Table III for explanations on the nature of the shown data and for the last caution sentence which applies here also for the $N = 551$ case in Experiment IIb.

N_t	$K_0 d^{-3}$	$\langle \rho_1 d^3 \rangle$	$\langle E/(N_1 + 1) \rangle$	$\beta \mu_1^*$	$\hat{\rho}_1$	$\hat{\rho}_1^{\text{eff}}$	r	$\beta p_w^{\text{br}} d^3$	$\beta p_w^{\text{fm}} d^3$	$\beta p^\infty d^3$	$\beta f_N d$
230	39.0698	0.0143(1)	0.0205(2)	-3.86(1)	0.827(8)	0.79(2)	0.96	0.0015(1)	0.0203(2)	0.0205	0.006(1)
300	39.0698	0.0155 (1)	0.0169(1)	-3.662(5)	1.003(6)	0.92(2)	0.92	0.0079(4)	0.0239(2)	0.0246	0.032(2)
370	39.0698	0.0163 (1)	0.0143(1)	-3.495(5)	1.186(8)	1.04(2)	0.88	0.021(1)	0.0274(3)	0.0290	0.088(5)
437	39.0698	0.0174 (1)	0.0118(1)	-3.303(7)	1.44(1)	1.19(2)	0.83	0.046(1)	0.0316(2)	0.0348	0.193(5)
500	39.0698	0.0203 (2)	0.00890(7)	-3.021(7)	1.91(1)	1.48(2)	0.77	0.087(3)	0.0375(3)	0.045	0.36(1)
550	39.0698	0.0270 (2)	0.00599(3)	-2.625(5)	2.83(1)	2.12(2)	0.75	0.156(2)	0.0485(5)	0.0652	0.63(1)
371	78.13968	0.0081 (1)	0.0286(3)	-4.189(1)	1.19(1)	1.09(2)	0.92	0.028(2)	0.0139(2)	0.0148	0.122(9)
438	78.13968	0.00884 (3)	0.0232(3)	-3.98(1)	1.46(2)	1.27(2)	0.87	0.058(1)	0.0162(1)	0.0181	0.252(7)
470	78.13968	0.0096 (1)	0.0199(2)	-3.83(1)	1.70(2)	1.44(2)	0.85	0.077(2)	0.0179(2)	0.0210	0.33(1)
501	78.13968	0.0116(2)	0.0156(2)	-3.58(1)	2.18(2)	1.74(2)	0.80	0.120(1)	0.0212(5)	0.0267	0.513(5)
551	78.13968	0.0198 (3)	0.00820(7)	-2.94(1)	4.13(4)	2.98(2)	0.72	0.233(3)	0.0333(3)	0.0488	0.98(1)

TABLE V. Equilibrium data on a brush of $N_f = 32$ filaments pressing against a fixed wall at density $\sigma_f d^2 = 0.32$ (Experiment III). N_t is the total number of monomers in the volume $V/d^3 = 1600$ which also contains 1000 MPCD solvent particles. See caption of similar Table III for explanations on the nature of the shown data. Note that $K_0/d^3 = 18.75352$ in the present case.

N_t	$\langle \rho_1 d^3 \rangle$	$\langle E/(N_1 + 1) \rangle$	$\beta \mu_1^*$	$\hat{\rho}_1$	$\hat{\rho}_1^{\text{eff}}$	r	$\beta p_w^{\text{br}} d^3$	$\beta p_w^{\text{fm}} d^3$	$\beta p^\infty d^3$	$\beta f_N d$
240	0.0274(1)	0.0130(1)	-3.035(7)	0.902(7)	0.79(2)	0.88	0.0029(1)	0.0441(2)	0.04461	0.0076(4)
290	0.0282(1)	0.01113(6)	-2.879(5)	1.053(6)	0.87(2)	0.83	0.0091(4)	0.0503(3)	0.05159	0.025(1)
350	0.0281(1)	0.00947(6)	-2.718(6)	1.238(8)	1.00(2)	0.81	0.0233(7)	0.0566(2)	0.05984	0.063(2)
430	0.0282(2)	0.00732(6)	-2.461(8)	1.60(1)	1.17(2)	0.73	0.0655(7)	0.0670(4)	0.07548	0.178(3)
490	0.0295(1)	0.00562(4)	-2.196(7)	2.09(1)	1.41(2)	0.67	0.121(1)	0.0756(5)	0.09539	0.315(3)
540	0.0369(2)	0.00370(3)	-1.778(8)	3.17(3)	1.98(2)	0.62	0.2060(5)	0.0933(7)	0.1365	0.509(3)

where the ideal solution function $f_N^{\text{id}} = \phi(L, T, \hat{\rho}_1)$ is given by Eq. (24) and where in the non ideal case, all interactions are taken into account by a renormalization of the effective reduced free monomer density leading to $\hat{\rho}_1^{\text{eff}}$. The comparison of Eq. (43) and Eq. (24) implies, assuming an effective state point independence of the mean wall force $\bar{f}_{z+k}(L)$ on a filament of size $z+k$, that

$$P_i(N_t, N_f, A, L, T) \cong P_i^{\text{id}}(L, T, \hat{\rho}_1^{\text{eff}}) \quad (44)$$

for all filament sizes ($i = 3, z^*$), where the ideal solution number density expressions are given by Eqs. (19), (20) and (21). We checked property Eq. (44) which was found to be reasonably verified, taken into account the relatively large statistical uncertainties on the densities for $i > z$.

The renormalized reduced free monomer density $\hat{\rho}_1^{\text{eff}}$ involves on one hand a pure solvent property, the product $f_1^\infty \rho_1^\infty$ directly linked by Eqs. (10) and (39) to the chemical potential μ_1^* and on the other hand the effectively i -independent ratio $r_i = f_{i-1}/f_i \approx r$ which is basically a measure of the free energy required to grow reversibly by one unit a filament of size $i-1$ within the bundle, at the state point considered. We have made a detailed analysis of the origin of the cost of free energy using Widom like formula derived originally to compute the incremental excess chemical potential of polymers $\mu_i^{\text{exc}} - \mu_{i-1}^{\text{exc}}$ in a polydisperse sample. [20] The outcome of our analysis is now briefly

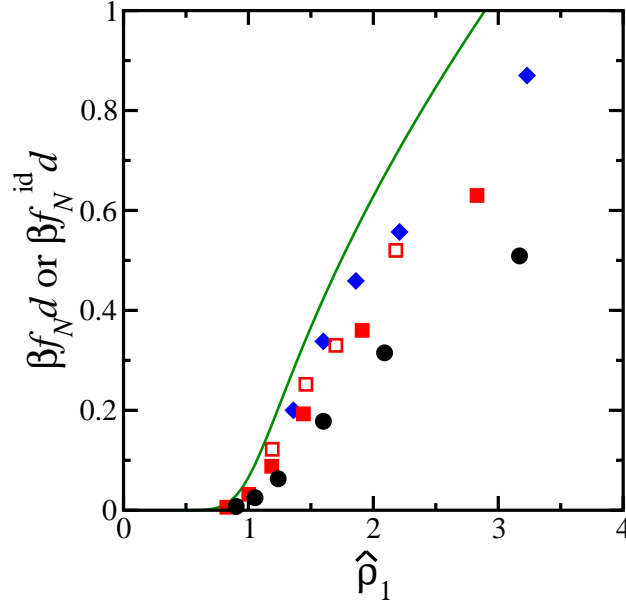


FIG. 4. Osmotic force per filament f_N as a function of $\hat{\rho}_1 = K_0 \rho_1^\infty f_1^\infty$ for simulation data corresponding to various surface densities $\sigma_f d^2 = 0.125$ (Experiment I, blue lozenges), 0.222 (red filled squares for Experiment IIa and red open squares for Experiment IIb), and 0.320 (Experiment III, black circles) compared to the ideal solution prediction of the force per filament f_N^{id} as a function of $\hat{\rho}_1$ based on the filament-wall microscopic model used in the bundle simulations.

summarized. First, we confirm that these independent r_i estimates are again found to be i independent at any state point where they reproduce, within a few percents, the ratio of activity coefficients given in Tables III, IV and V, based on the characteristic lengths of the exponential size distribution of the filaments at each state point (Eq.(36)). The free energy cost involves the reversible work of growing the filament against repulsive forces coming both from the other filaments and from the free monomers within the solution. When looking at the results within any experiment series (I, IIa, IIb or III), we find that, with $\hat{\rho}_1$ increasing (see data in Tables), the observed systematic decrease of r can be traced as originating from a combination of both types of repulsive interactions. However, when comparing data from experiments I and IIb which have different grafting densities but the same equilibrium constant K_0 , we find that for two state points taken at the same $\hat{\rho}_1$ (μ_1) value, the global r factor is lower for the denser brush (exp IIb) solely, as a result of the more important interfilament interactions in the denser denser brush case. This can be observed by comparing cases $N_t = 550$ in experiment I (Table III) and $N_t = 501$ in experiment IIb (Table IV) for which we have the same $\hat{\rho}_1 \cong 2.2$. When comparing experiments IIa and IIb with the same grafting density but with equilibrium constants K_0 differing by a factor two, one observes for a given similar value of $\hat{\rho}_1$ in both experiments that to the highest K_0 value corresponds the largest r value solely as a result of the lower free monomers density, as the contribution to r from inter-filament interactions remain similar at the same grafting density. This can be seen by comparing in Table IV, the case $N_t = 437$ of experiment IIa and the case $N_t = 438$ of experiment IIb for which $\hat{\rho}_1 \approx 1.45$.

The above discussion concerns a large set of simulations considered for different grafting densities σ_f , different equilibrium constants K_0 and different free monomer chemical potential μ_1 . These simulations deal however with a single specific box length $L/d = 16$, a single temperature T , a single persistence length l_p and a specific filament-wall model $U_w(r)$ and it must be added that the filament arrangement within the bundle is also specific as all seeds (say one of the two first monomers anchored in the left wall) are located within a strictly planar wall interface. In that context, the functional form of $f_N^{\text{id}} = \phi(L, T, \hat{\rho}_1)$ shown in Fig. 4 and hence of $f_N = \phi(L, T, \hat{\rho}_1^{\text{eff}})$ in the non ideal conditions of the simulations, should be highly specific to the choice of all these parameters.

Reasoning on the L dependence of the force in the ideal bundle case is relatively straightforward [17]. Explicit calculations of f_N^{id} show pronounced local fluctuations of period d for L variations within the monomer size, the general shape of the fluctuations repeating with some damping effect as L increases over a few d distances (remaining within the regime $L \ll l_p$). The shape of these fluctuations is illustrated in the inset of Fig. 6 for the model Hamiltonian used for our simulations. By averaging Eq. (24) at a given $\hat{\rho}_1$ over one monomer size interval [$L - d/2 < L' < L + d/2$],

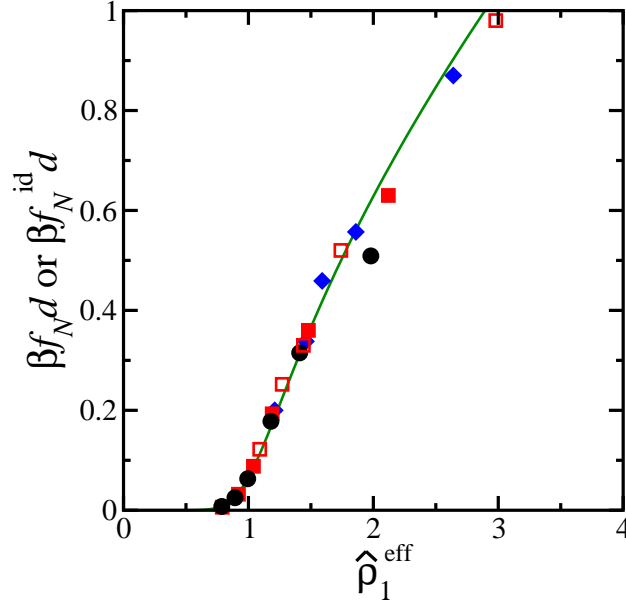


FIG. 5. Osmotic force per filament f_N as a function of $\hat{\rho}_1^{\text{eff}}$ for simulation data corresponding to various surface densities $\sigma_f d^2 = 0.125$ (Experiment I, blue lozenges), 0.222 (red filled squares for Experiment IIa and red open squares for Experiment IIb), and 0.320 (Experiment III, black circles) compared to the ideal solution prediction of the force per filament f_N^{id} as a function of $\hat{\rho}_1$ based on the filament-wall microscopic model used in the bundle simulations.

one gets trivially

$$\beta f_N^{\text{id,av}}(L, \hat{\rho}_1) = \frac{1}{d} \ln \left[\frac{D(L + 0.5d, \hat{\rho}_1)}{D(L - 0.5d, \hat{\rho}_1)} \right] \quad (45)$$

which can be computed using Eq. (21). In Fig. 6, this average function $\beta f_N^{\text{id,av}}(L, \hat{\rho}_1)$ for $L/d = 16$ is shown together with the specific $L/d = 16$ expression of $f_N^{\text{id}} = \phi(L, T, \hat{\rho}_1)$ already shown in the two previous figures. Moreover, for comparison, the ratchet model force Eq. (1) is also shown for $\hat{\rho}_1 > 1$. It turns out that the average force per filament (in the ideal bundle case) is not quantitatively very different from Eq. (1). The distinction between both expressions can be analyzed [17] by noting that after isolating a $\hat{\rho}_1$ term in the fraction of the right hand side of Eq. (45), it remains a ratio of two similar expressions which are related by the property that any $\alpha_i(L + d/2)$ term in the numerator of the fraction is close to a corresponding $\alpha_{i-1}(L - d/2)$ term in the denominator of the fraction as they correspond to the same universal function $\tilde{Z}(\tilde{\eta})$ [18] computed for two reduced compression variables $\tilde{\eta}$ (Eq. (26)) differing in relative terms by $2d/L_{ci}$. The universality observed in terms of $\hat{\rho}_1^{\text{eff}}$ for the particular investigated value of $L/d = 16$ in Fig. 5 and the observation of the weak (L, l_p) dependence of $f_N^{\text{id,av}}$ suggest that non ideal systems should be characterized by an average reduced force $\beta f_N^{\text{av}} d \approx \ln \hat{\rho}_1^{\text{eff}}$. We will come back on this issue in Section V.

C. Filament size kinetics

During all the equilibrium simulations, the number of successful polymerization and depolymerization events has been recorded. The polymerization and depolymerization rates per active end, respectively U_i and W_i , for size i filaments are shown in Fig. 7 for experiments of series I, namely those at the lowest surface grafting density. Only values relative to filament sizes present in significant amount are shown in the figure. We remind here some qualitative features of the chemical step algorithm, all details being found in the original Ref. [16] To get a polymerization step, a free monomer must be present for some time at direct proximity of an active end of a filament. As long as the monomer is at proximity, with some probability per unit time, a polymerization attempt can be tried. This attempt consists in transferring spatially this monomer to a tiny region of space where the monomer fits the intramolecular structure, i.e. is located at a distance close to d from the last monomer of the filament and forms a virtual relatively straight trimer with the two last monomers of the filament. This topological and spatial move is then the object of an acceptance/rejection sampling linked to the possible overlap of the displaced monomer with the other monomers and/or with the wall.

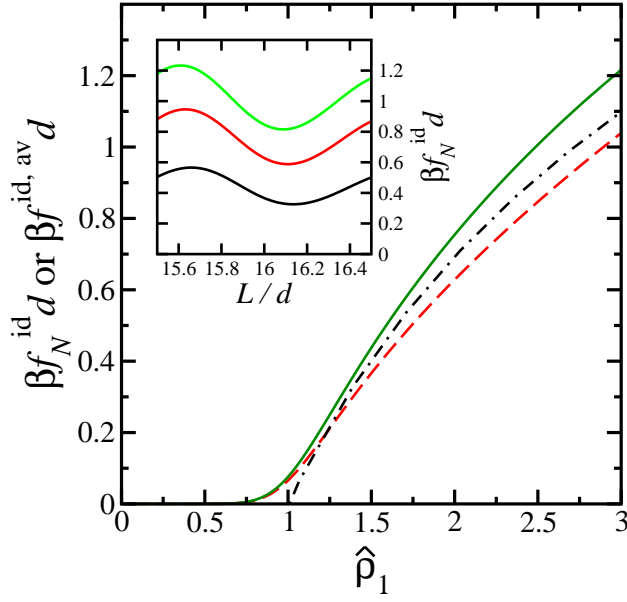


FIG. 6. Local reduced force $\beta f_N^{\text{id}} d$ (red dashed curve) and local reduced average force $\beta f_N^{\text{id,av}} d$ (green continuous curve) exerted by the right wall located at gap distance $L/d = 16$ on one filament anchored normally at the left wall and growing towards the right, as a function of $\hat{\rho}_1$, for the filament model (with $l_p = 250d$) and for the filament-wall interaction model which are used in bundle simulations. The black dash-dotted curve shows $\beta f_N^{\text{id}} d = \ln \hat{\rho}_1$ predicted by Eq. (1). Inset: same local reduced force $\beta f_N^{\text{id}} d$ for a right wall position varying between $L/d = 15.5$ and $L/d = 16.5$. The three curves (from bottom upwards) correspond to free monomer reduced number densities $\hat{\rho}_1 = 1.5$, $\hat{\rho}_1 = 2.0$ and $\hat{\rho}_1 = 2.5$.

For the reverse case, any end-monomer of a filament is essentially all the time available for a depolymerization step. With some probability per unit time, an attempt is made to detach and relocate instantaneously the freed monomer at proximity of the new filament end. This depolymerization trial step is then subjected to an acceptance/rejection on the basis of possible overlap with the other monomers and with the wall. Imposed algorithm micro-reversibility demands that

$$P_i U_i = P_{i+1} W_{i+1} \quad (46)$$

and this property is found to be systematically satisfied in all cases, showing simply the correct implementation of our algorithm. [16] The property in Eq. (46) combined with the observed exponential profile of P_i following Eq. (35), implies that $U_i/W_{i+1} \approx \hat{\rho}_1^{\text{eff}}$ in the regime $i < z = 15$.

Figure 7 shows that in experiment series I, for filament sizes ($i \leq z = 15$) for which direct interaction with the wall is not possible, the polymerizing rates U_i (for $i \leq (z - 1) = 14$) and depolymerizing rates for W_i ($i \leq z = 15$) are reasonably constant, and we denote by U_0 or W_0 the average values. For the different state points, we get for the pairs of (wall) unperturbed rates ($U_0 u_t, W_0 u_t$) the values 0.0018/0.00148 ($N_t = 450$), 0.0020/0.00136 ($N_t = 500$), 0.0022/0.00135 ($N_t = 520$) and 0.00245/0.00133 ($N_t = 550$). As expected from the combination of Eqs. (46) and (35), the ratio $U_0/W_0 = \hat{\rho}_1^{\text{eff}}$ and indeed the values of this ratio (1.22 ($N_t = 450$), 1.47 ($N_t = 500$), 1.63 ($N_t = 525$) and 1.84 ($N_t = 550$)) are always compatible with the $\hat{\rho}_1^{\text{eff}}$ estimates reported in Table III.

Within the series of experiments where only N_t changes from one state point to the other, while all other parameters including in particular the equilibrium constant K_0 are the same, one notes a small decrease of W_0 with N_t increasing as a result of a decrease in the depolymerization step acceptance probability due to increasing volume fraction. The fast increase of U_0 with N_t is related to the first order character, for a given filament end, of the polymerizing reaction as suggested by the systematic increase of $\langle \rho_1 \rangle$ with increasing N_t (see Table III).

All the curves in Fig. 7 show the same trend for the evolution of the (de)polymerization rates as the wall is approached. One observes that W_i , involving the detachment and re-positioning of the freed monomer at proximity of the new filament end, is only slightly affected by the presence of the wall repulsive potential. The weak decrease of W_i with respect to W_0 for $i > z$ must be related to a decrease of the acceptance probability of the attempted depolymerizing step, as a result of some additional overlap from the wall when the random relocation of the freed monomer happens along the end-filament longitudinal direction towards the wall. On the contrary, the polymerization step is strongly affected by the wall presence, as the result of the combination of two effects tending to lower U_i . The

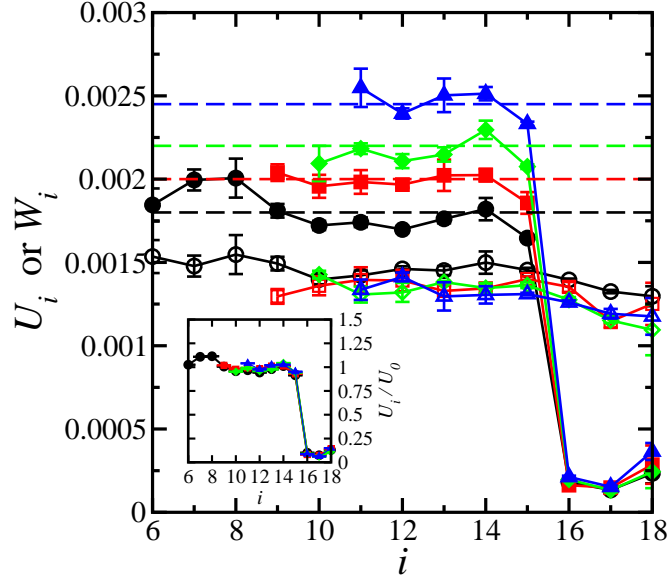


FIG. 7. Polymerization rate U_i and depolymerization rate W_i (in units u_t^{-1}) for filaments of various sizes i in the series of experiments I, $N_t = 450$ (circles), 500 (squares) and 525 (lozenges) and 550 (triangles). Only points known with reasonable statistics (corresponding to significant P_i values) are indicated, with filled symbols for U_i and empty symbols for W_i . The error bars being set to one σ (estimated from four independent runs per experiment). Continuous lines are shown to facilitate data observation. Estimated bulk constant values U_0 (see text) are indicated by horizontal dashed lines. The inset shows the polymerization rates for all values of i in their rescaled form U_i/U_0 .

attempt probability must be lowered by the wall presence as the obstacle produces a decrease of the space available to a free monomer to get close to the active end and so only a lateral approach for the incoming reactive monomer is possible. The second cause is linked to the acceptance probability part as the tiny portion of space in which the reactive monomer is supposed to attach to maintain a limited additional intramolecular potential energy, will very often have a strong overlap with the wall highly repulsive region. We note that the wall potential energy climbs from $U_w = 0$ at the cutoff distance $x_c/d = 1.2$ from the wall up to $U_w/k_B T = 5.8$ when the distance to the wall is decreased by $d/2$ at $x = 0.7d$.

The decrease of U_i for $i \geq z$ can be estimated quantitatively starting from the micro-reversibility, Eq. (46), applied for arbitrary k , to $i = z + k - 1$,

$$\begin{aligned} U_{z+k-1} &= \frac{P_{z+k}}{P_{z+k-1}} W_{z+k} \\ &\approx \frac{\alpha_{z+k}}{\alpha_{z+k-1}} \rho_1^{\text{eff}} W_0 \approx \frac{\alpha_{z+k}}{\alpha_{z+k-1}} U_0 \end{aligned} \quad (47)$$

where we have assumed that $W_{z+k} \approx W_0$ and approximated the size distribution according to Eq. (44). Using the potential of mean force introduced in Eq. (25), one has

$$U_{z+k-1} = \exp(-\beta(w_{z+k} - w_{z+k-1})) U_0 \quad (48)$$

which expresses that the rate of polymerization U_{z+k-1} is the unperturbed rate U_0 times the Boltzmann factor implying the difference in confinement free energy for the same wall position, between filaments of size $z + k$ and $z + k - 1$. Being specific, the use Eq. (47) with $\alpha_z = 1$ and other α_{z+k} values ($k \geq 1$) mentioned in Sec. IV A, leads to $U_{15} = 0.925U_0$, $U_{16} = 0.127U_0$, $U_{17} = 0.120U_0$ and $U_{18} = 0.19U_0$. These estimates are in quite good agreement with all data of experiment I in Fig. 7 which suggest a small systematic decrease of U_{15} followed by a strong decrease for U_{16} and U_{17} followed by a slight but significant increase for U_{18} . The prediction of Eq. (47) or of Eq. (48) that U_i/U_0 for $i \geq z$ is only dependent on the α 's is shown in inset in Fig. 7 and appears to remain valid in these slightly non-ideal conditions.

The behavior of chemical rates in the other series of experiments remains similar to what was shown for Experiment I. However, one notes especially in the highest density series of experiments III, some systematic variations of U_i and W_i of the order of 20-30 percent within the observed size i domain below the region of direct wall influence. This

trend however coexists with the exponential distribution of the filament size probabilities Eq. (35) and with the micro-reversibility requirement Eq. (46). The concept of unique rates U_0 and W_0 appears thus less appropriate in denser bundles and a more detailed analysis of these more complex inhomogeneous systems would be needed.

V. DISCUSSION AND PERSPECTIVES

Using the recently proposed simulation methodology to model the structure and dynamics of self-assembling stiff filaments at a mesoscopic level, [16] we have investigated the dynamics of a bundle of grafted living filaments growing against a fixed wall. In this Molecular Dynamics approach, each active end of the filament is subject to explicit local (de)polymerizations and monomer exchange with an embedding free monomer solution. Such a situation is reminiscent of cytoskeletal biofilament networks and more specifically of the actin filopodia where a set of parallel double-stranded actin filaments push on the cell membrane as a result of dominant end-filament polymerizations. However, being motivated by a generic molecular level understanding of the chemo-mechanical coupling, our strategy has been to exploit a minimum model of a confined solution of interacting spherical free monomers able, in presence of set of permanent grafted filament seeds, to dynamically self-assemble into an equivalent number of grafted wormlike chains with fluctuating contour length. For such model, crucial parameters like filament persistence length, chemical reaction rates, grafting density, diffusivity of free monomers, etc can be independently fixed and tuned. This enables us to gain a general understanding of the physics behind the phenomena where chemical energy is transduced to develop mechanical forces and work, a basic phenomenon at the root of cell motility.

Specifically, for a large class of state points differing by the grafting density and by the total number of monomers in the confined volume, we have simulated a bundle of 32 filaments grafted normally to a planar surface and hitting a fixed obstacle wall, parallel to the grafting wall, with gap width much smaller than the filament persistence length. For each state point, the simulations were invariably started from a set of 32 grafted seeds and a state-point specific number of free monomers filling the available free space. As the simulation process is launched, the filaments start growing and the bundle spontaneously evolves towards an equilibrium situation for the bundle/free monomer solution system. Subsequent long microscopic trajectories were then exploited to probe the structure and some dynamical fluctuations of each investigated state point of this grafted bundle network.

As a first outcome of our work, the thermodynamic and statistical mechanics frameworks relevant to a bundle of living and interacting filaments in chemical equilibrium with a solution of free monomers is established in Sec. II. Our approach, inspired by statistical mechanics concepts developed long time ago by T. L. Hill for reactive ideal and non-ideal mixtures, [19] is based on a reactive canonical ensemble and an associated free energy where both the number of filaments N_f and the total number of monomers N_t are fixed, in addition to the temperature T and the geometrical dimensions of the confined volume, namely the gap width L and transverse section area A . Section II A introduces formally the correcting factors for intermolecular interactions, namely the activity coefficients f_1 (for free monomers) and f_i (for grafted filaments of size i) and defines also a series of wall factors $\alpha_i(L)$ as correction terms to the ideal partition function of a single unconfined grafted filament of size i . To the free monomer chemical potential $\mu_1(N_t, N_f, T, A, L)$ in the bundle system can be associated a free monomer solution reservoir in equilibrium with the bundle solution, having thus a number density ρ_1^∞ and n free monomer activity coefficient f_1^∞ related by $\mu_1 = \ln(f_1^\infty \rho_1^\infty)$. The osmotic force exerted by the bundle on the fixed wall, which is at the heart of the present work, must be strongly related to the distribution of filament sizes P_i . In Sec. II A, the size probabilities are related by Eq. (17) which summarizes how wall factors, activity coefficients of filaments and chemical potential μ_1 of the free monomer reservoir in equilibrium with the bundle interfere to produce the equilibrium distribution of filament sizes. This framework is essential to discuss on equal footing theoretical predictions in the ideal bundle approach and all results obtained by our simulations in non-ideal conditions.

Precisely, a decisive advantage of our choice for a bundle network is that an exact treatment is possible for the corresponding ideal solution version of our confined bundle model. The latter follows by simply neglecting all intermolecular interactions while keeping unaltered from the full microscopic model, all intramolecular and wall interactions. The predictions for this ideal solution treatment (where all activity coefficients are set to unity), have already been detailed elsewhere. [17] Given the importance of the ideal bundle case as a reference point, the salient properties of the ideal bundle case were summarized in Sec. II B. The distribution of filament sizes is exponential $P_i \propto \exp[i \ln(\rho_1 K_0)]$ as long as the sizes of the filaments are sufficiently small to avoid direct contact with the wall. In the size distribution expression, K_0 is the ideal solution (de)polymerization equilibrium constant of the active free end (in absence of confinement effects) and ρ_1 is the free monomer number density. Their product $\hat{\rho}_1 = \rho_1 K_0$ provides the criterium for subcriticality $\hat{\rho}_1 < 1$ where depolymerization dominates or for supercriticality $\hat{\rho}_1 > 1$ where free ends of filaments are growing on average. In the supercritical case, the equilibrium size distribution is an increasing function of the size up to the point where the wall interactions start inhibiting the occurrence of longer filament sizes, their probability P_i being rescaled by the corresponding wall factor $\alpha_i(L; l_p)$ depending on the filament size, the gap width and the

filament persistence length. The shape of this part of the distribution relative to filament sizes hitting the wall, results from a subtle balance between two opposite trends: the tendency for filaments to grow by polymerization and the price to pay for compressional free energy $w_i(L; l_p) = -k_B T \ln \alpha_i(L; l_p)$ associated to the overall bending of filaments with contour length $L_{ci} > L$. We note that the properties of these wall factors and their associated compression potentials of mean force have been recently studied for grafted wormlike chains hitting a hard wall. [18] In general, these wall factors (which need to be computed by single filament Monte-Carlo sampling [17]) and the reduced free monomer density $\hat{\rho}_1$ provide the basic ingredients to establish at the same time the filament size distribution and the explicit expression of the compressive force $f_N^{\text{id}}(L, \hat{\rho}_1)$ exerted by each independent filament on the fixed obstacle wall.

Returning now to the simulated non-ideal bundles, we first point out that for the different state points differing by the grafting density and by the total number of monomers, we have systematically estimated the equilibrium free monomer chemical potential μ_1 by a particle insertion method adapted to the present reactive system which is derived in detail in the Supplementary Material. This allows to compare more easily bundle properties at different grafting density, in equilibrium with the same free monomer reservoir. For each state point, the structure of the bundle, the inhomogeneous free monomer density and the force exerted by the set of self-assembled stiff living filaments on the obstacle have been estimated. In addition, we have also recorded the effective rates of polymerization U_i and depolymerization W_i for both short filaments (not hitting the wall) and for long filaments which are directly in contact with the wall. We have analyzed how these rates are influenced by the interactions between filaments and free monomers and by the obstacle confinement. This large set of results, regrouped in Tables II, III, IV and V are produced at many state points on the basis of a unique microscopic model for which we know exactly the properties within the ideal solution approximation. This allows us to highlight the various influences of interactions or of confinement on the living filament bundle properties and this analysis is a major original outcome of our work.

The main result of our simulations on non ideal bundles is that the same functional form applies in ideal and non-ideal situations, when studying the dependence of structural properties on the free monomer density. The explicitly known $\hat{\rho}_1$ dependence of the wall force per filament in the ideal case at a given gap width L , namely $f_N^{\text{id}} = \phi(\hat{\rho}_1; L, T)$, turns out to be valid to describe the force per filament for a bundle with strong inter-filament and/or strong filament-free monomers interactions, provided $\hat{\rho}_1$ is replaced by an appropriate renormalized reduced free monomer density $\hat{\rho}_1^{\text{eff}}$. Pragmatically estimated from the exponential size distribution of filaments which are not interacting with the wall, its thermodynamic interpretation could be traced to the combination $\hat{\rho}_1^{\text{eff}} = K_0 f_1^\infty \rho_1^\infty f_{i-1}/f_i$ where the ratio f_{i-1}/f_i is the effectively i -independent quantity within the free (non hitting) filaments regime. With our choice of purely repulsive intermolecular interactions between filaments, the average wall force per filament appears to decrease as the grafting density increases for a series of bundles exposed to the same free monomer reservoir chemical potential. This property is coherent with the opposite trend predicted theoretically for a bundle of attractive filaments. [10] In summary, we observed in our simulated bundles in supercritical conditions, that the repulsive interactions weaken the effective polymerization tendency by slowing down the static exponential growth of the short filaments distribution, an effect directly coupled to the similar effective weakening of the wall osmotic pressure exerted by the filaments.

Coming back to general aspects valid for both ideal and non ideal bundles, it must be stressed that the wall forces per filament f_N discussed in this work concern a unique and (ensemble) fixed value of L . Ideal bundle theory [17] indicated that the force $f_N^{\text{id}}(L; \hat{\rho}_1, T)$ for a single filament varies quite strongly with L over a single monomer size interval $L - d/2, L + d/2$, basically as a result of the strong variations with L of the populations of the different filament chemical species hitting the wall and as a result of the variation of the wall factors α_i with L . These variations of f_N tend to be replicated periodically in space with a period d at larger L values, but with some systematic damping effect related to the progressive increase of the ratio L/l_p . However, if the force is averaged over a L window of size d , a result close to Eq. (1) is recovered [17] suggesting that the force F mentioned in ratchet theories for the stalling force needed to stop polymerizing filaments [1] must be interpreted as an average force whose work Fd over a distance d has to be identified with the integral over a L interval of size d of the fixed L equilibrium force discussed we have been measuring in our simulations. Similarly, the L dependent force cannot be related directly to the force measured in an optical trap experiment [4] where a mobile wall (bead) is subject to both the bundle pressure and the restoring trapping force. The unavoidable Brownian motion of the confining mobile wall (bead) in the trap (of the order of $\sqrt{k_B T/k_{\text{trap}}}$ lead to fluctuations of the effective size of the tested bundle which are larger than d (in the experiment on actin, $d = 2.7$ nm and $\sqrt{k_B T/k_{\text{trap}}} \cong 23$ nm), hence the quantity measured should again be an average of the filament wall force over a range larger than d . In principle, according to our results on non-ideal bundles, a plausible estimate of such an average wall force per filament in a non-ideal case should approach $(k_B T/d) \ln(\hat{\rho}_1^{\text{eff}})$.

Finally, our simulations give access to kinetics aspects for chemical reactions involving the grafted filaments. Given our algorithm where attempted reaction steps are subsequently either refused or accepted according to the associated microscopic energetic changes, the polymerization and depolymerization rates are affected by both the intermolecular interactions and by the confinement potential. We found in the low grafting surface density case that the rates are i -independent in the short (non hitting) filament regime, but are strongly dependent on the state point with the property $U_0/W_0 = \hat{\rho}_1^{\text{eff}}$ (where U_0 and W_0 denote these polymerizing and depolymerizing homogeneous rates

respectively), which is a direct consequence of microreversibility and the insensitivity to i of the rates, given the exponential filament size distribution profile discussed earlier. The wall effect on these rates for filament sizes hitting the wall was analyzed and found to be rather weak for depolymerization but on the contrary spectacular for the polymerization rates. A first order approximation for these rates for hitting filament sizes was suggested as $W_i = W_0$ and $U_i = (\alpha_{i+1}/\alpha_i)U_0$, which again take into account both the state point influence (through the bulk rates U_0 and W_0) and the wall influence (through the wall factors).

In conclusion, the ensemble of structural and dynamic results we have obtained for a system of grafted and interacting living filaments at equilibrium can be rationalized in terms of a reference state, namely an ideal confined bundle of living filaments, to which non-ideality corrections can be identified. Beyond this important point, the methodology followed to get these results suggests that we have at disposal a robust machinery able to drive our living system spontaneously, thanks to a combination of free monomer diffusive steps and (de)polymerizing chemical steps, to the equilibrium state of a living filament network, under the constraints of a well defined statistical mechanics ensemble. It suggests that the methodology could be extended to more complex filament networks (e.g. branched networks, flexible membranes obstacles, distinction between hydrolyzed and non hydrolyzed actin complexes etc) at the price of an increase in the number of chemical species for the building blocks and at the price of the consideration of a larger set of competing chemical reactions. Such complex networks are already studied by biophysicists, [7, 21, 22] generally in non-equilibrium conditions, on the basis of ad hoc stochastic rules regarding various probabilities for filament branching, filament capping or filament elongation by polymerization, and on the basis of hypotheses on how a wall force affects these probabilities and how the load force exerted on the wall must be distributed among all hitting filaments. These stochastic network simulations usually deal with wider non-equilibrium dynamical properties like the force-velocity relationship for a network pressing against a mobile wall. Our methodology is ripe not only for extensions towards more complex networks (at equilibrium) but can also be applied to dynamical network properties by releasing the fixed wall constraint while exerting an external load instead. Work along these lines are in progress. It should help interpreting the chemo-mechanical coupling for a simple network of parallel living filaments pushing on a mobile wall, a problem addressed in recent theoretical works, either directly for the bundle case [8] or for more complex actin networks. [21]

ACKNOWLEDGMENTS

The authors wish to thank M. Baus, G. Ciccotti, J.-F. Joanny, P. B. S. Kumar, D. Lacoste and C. Pierleoni for useful discussions about the present work. They warmly thank G. Destrée for invaluable technical help. S. Ramachandran acknowledges financial help from the BRIC (Bureau des Relations Internationales et de Coopération) of the Université Libre de Bruxelles. J.-P. R. thanks P. B. S. Kumar for hosting him at IIT Madras where this work was completed.

Appendix A: Derivation of the chemical potential μ_1 of free monomers in chemical equilibrium with the anchored bundle within the reacting canonical ensemble

This appendix establishes the final expression given by Eq. (41) which allows us to compute operationally, via a Widom-like method, the chemical potential of the free monomers within our reacting mixture at chemical equilibrium. From the formal definition in Eq. (10), we can write $\mu_1 = F(N_t + 1, N_f, A, L, T) - F(N_t, N_f, A, L, T)$, and thus, using the short symbol $Q(N_t, X)$ for the reactive canonical ensemble partition function where X denotes the remaining set of independent variables $X = (N_f, A, L, T)$, one has

$$\mu_1(N_t, X) = -k_B T \ln \frac{Q(N_t + 1, X)}{Q(N_t, X)}, \quad (\text{A. 1})$$

$$Q(N_t, X) = \sum_{N_1, \{N_i\}}^{N_t} \frac{1}{h^{3N_t} N_1! \dots N_i! \dots} \int d\Gamma^{N_t} \exp[-\beta H(N_1, \{N_i\})], \quad (\text{A. 2})$$

$$Q(N_t + 1, X) = \sum_{N'_1, \{N'_i\}}^{N_t+1} \frac{1}{h^{3(N_t+1)} N'_1! \dots N'_i! \dots} \int d\Gamma^{N_t+1} \exp[-\beta H(N'_1, \{N'_i\})], \quad (\text{A. 3})$$

where the sum in Eq. (A. 2) and the sum in Eq. (A. 3) imply in each case the sum over all distinct sets of integer values (starting from 0) such that the total number of filaments is N_f while the total number of monomers is N_t in the first case and $N_t + 1$ in the second case. Note that the possible values for the number of species of the same kind are represented by unprimed quantities for N_t (N_1, N_3, \dots) and by primed quantities for $N_t + 1$ (N'_1, N'_3, \dots).

To illustrate next developments, the table below provides the complete set of distinct arrangements of populations satisfying $N_f = 2$ and either $N_t = 9$, $N_t = 10$ or $N_t = 11$. This table shows that if one knows all distinct sets (N_1, N_3, \dots) for one pair of values of N_f and N_t , the whole set of possibilities N'_1, N'_3, \dots corresponding to the pair of values N_f and $N_t + 1$, can be divided into two classes

- those for which $N'_1 \geq 1$ which are in one-to-one correspondence with the same set of filament populations in the previous column for N_t arrangements, with $N'_3 = N_3, \dots, N'_i = N_i, \dots$, while $N'_1 = N_1 + 1$.
- those for which $N'_1 = 0$ which correspond to all distinct topological ways to distribute $N_t + 1$ monomers into N_f filaments without any free monomer left.

On the basis of this observation, one can rewrite Eq. (A. 1) for a set of $N_t + 1$ monomers (in terms of N'_1, N'_3, \dots sets) in separating the two types of contributions distinguished above, the first term being rewritten automatically as a sum over all distinct population sets of the N_t case (in terms of the N_1, N_3, \dots sets and the second being limited to all sets with $N'_1 = 0$. This gives

$$Q(N_t + 1, X) = Q_1 + Q_2, \quad (\text{A. 4})$$

$$Q_1 = \sum_{N_1, \{N_i\}}^{N_t} \frac{1}{h^{3(N_t+1)} (N_1 + 1)! \dots N_i! \dots} \int d\Gamma^{N_t+1} \exp[-\beta H(N_1 + 1, \{N_i\})], \quad (\text{A. 5})$$

$$Q_2 = \sum_{\{N'_i\}}^{N_t+1} \frac{1}{h^{3(N_t+1)} N'_3 \dots N'_i! \dots} \int d\Gamma^{N_t+1} \exp[-\beta H(N'_1 = 0, \{N'_i\})] \quad (\text{A. 6})$$

where the sum in Q_2 implies a number of N_f filaments of size between $i = 3$ and $i = z^*$ and a total number of monomers $N_t + 1$ satisfying $N_t + 1 = \sum_i i N'_i$. We now need to exploit the partition indicated in Eq. (A. 4) to evaluate the ratio of partition functions Q_1/Q and Q_2/Q (see Eq. (A. 1)) and we now treat both cases successively.

Looking at Q_1 as defined by Eq. (A. 5), we isolate in each term of the sum one free monomer (considered as an extra monomer which will be specified by six coordinates written as Γ_{ex}) in the integrals and we also isolate the corresponding spatial coordinate in the Hamiltonian where ΔH_{ex} contains all kinetic and potential terms which need to be added when this extra particle is incorporated to the system,

$$Q_1 = \sum_{N_1, \{N_i\}}^{N_t} \int d\Gamma^{N_t} \frac{1}{h^3 (N_1 + 1)} \int d\Gamma_{\text{ex}} \exp[-\beta \Delta H_{\text{ex}}] \frac{1}{h^{3N_t} N_1! \dots N_i! \dots} \exp[-\beta H(N_1, \{N_i\})]. \quad (\text{A. 7})$$

Inspection of the ratio $Q_1/Q(N_t, X)$ indicates that it corresponds to an equilibrium average over the (N_t, X) ensemble, namely

$$\frac{Q_1}{Q(N_t, X)} = \left\langle \frac{1}{h^3 (N_1 + 1)} \int d\Gamma_{\text{ex}} \exp[-\beta \Delta H_{\text{ex}}] \right\rangle_{N_t, X}, \quad (\text{A. 8})$$

$$= \frac{V(2\pi M k_B T)^{3/2}}{h^3} \left\langle \frac{1}{(N_1 + 1)} \int_0^1 ds_{\text{ex}}^3 \exp[-\beta \Delta U_{\text{ex}}] \right\rangle_{N_t, X}, \quad (\text{A. 9})$$

$$= \frac{V}{\Lambda^3} \left\langle \frac{1}{(N_1 + 1)} \int_0^1 ds_{\text{ex}}^3 \exp[-\beta \Delta U_{\text{ex}}] \right\rangle_{N_t, X}, \quad (\text{A. 10})$$

where the integrations over the extra particle degrees have been either performed explicitly for the momenta or written in terms of reduced coordinates \mathbf{s}_{ex} (using a reduction by the box dimensions) for their coordinates. ΔU_{ex} is the potential energy increase when the extra particle is added to the set of N_t monomers of the system associated to the ensemble on which average is taken. Finally, M is the monomer mass and Λ is the de Broglie wave length.

Q_2 in Eq. (A. 6) has the structure of a partition function relative to a subset of microscopic configurations of the original ensemble that could be written as $Q^0(N_t + 1, X)$. Here the superscript indicates that only the subset of microscopic configurations with $N_1 = 0$ are included. Using this new notation, we rewrite the ratio Q_2/Q as

$$Q_2/Q = \frac{Q^0(N_t + 1, X)}{Q(N_t, X)} = \frac{Q^0(N_t + 1, X)}{Q^0(N_t, X)} \frac{Q^0(N_t, X)}{Q(N_t, X)} \quad (\text{A. 11})$$

$$= \frac{Q^0(N_t + 1, X)}{Q^0(N_t, X)} P(N_1 = 0; N_t, X). \quad (\text{A. 12})$$

TABLE VI. List of distinct population possibilities for a reacting system with a total of N_t monomers and a total of N_f filaments arranged in N_1 free monomers, N_3 filaments of length 3, \dots , N_i filaments of length i , \dots for three successive values of N_t and same N_f . N_1 values are indicated explicitly, while only non zero populations of filaments of size i are indicated. All distinct possibilities are grouped for one specific value of N_1 in order to appreciate the links between sets relative to consecutive values of N_t .

$N_t = 9 \quad N_f = 2$	$N_t = 10 \quad N_f = 2$	$N_t = 11 \quad N_f = 2$
		$N_1 = 0 \left\{ \begin{array}{l} N_5 = N_6 = 1 \\ N_4 = N_7 = 1 \\ N_3 = N_8 = 1 \end{array} \right.$
	$N_1 = 0 \left\{ \begin{array}{l} N_5 = 2 \\ N_4 = N_6 = 1 \\ N_3 = N_7 = 1 \end{array} \right.$	$N_1 = 1 \left\{ \begin{array}{l} N_5 = 2 \\ N_4 = N_6 = 1 \\ N_3 = N_7 = 1 \end{array} \right.$
$N_1 = 0 \left\{ \begin{array}{l} N_3 = N_6 = 1 \\ N_4 = N_5 = 1 \end{array} \right.$	$N_1 = 1 \left\{ \begin{array}{l} N_3 = N_6 = 1 \\ N_4 = N_5 = 1 \end{array} \right.$	$N_1 = 2 \left\{ \begin{array}{l} N_3 = N_6 = 1 \\ N_4 = N_5 = 1 \end{array} \right.$
$N_1 = 1 \left\{ \begin{array}{l} N_4 = 2 \\ N_3 = N_5 = 1 \end{array} \right.$	$N_1 = 2 \left\{ \begin{array}{l} N_4 = 2 \\ N_3 = N_5 = 1 \end{array} \right.$	$N_1 = 3 \left\{ \begin{array}{l} N_4 = 2 \\ N_3 = N_5 = 1 \end{array} \right.$
$N_1 = 2 \quad N_3 = N_4 = 1$	$N_1 = 3 \quad N_3 = N_4 = 1$	$N_1 = 4 \quad N_3 = N_4 = 1$
$N_1 = 3 \quad N_3 = 2$	$N_1 = 4 \quad N_3 = 2$	$N_1 = 5 \quad N_3 = 2$

In the thermodynamic limit, the probability $P(N_1 = 0; N_t, X)$ for our system in chemical equilibrium to be in any state where $N_1 = 0$ is vanishingly small. We checked that in our bundle simulations with a few hundreds monomers, the fluctuation δN_1 around the mean $\langle N_1 \rangle$ remains typically of the order of 10 – 15 percent of this mean, indicating that finite size effects on $P(N_1 = 0; N_t, X)$ remain negligible. We note that this very small probability is multiplied by a term which has the same structure as the Q_1/Q term and which could be expressed in terms of the insertion probability of a filament of size $i + 1$ in replacement of a filament of size i in the sub-ensemble of cases where $N_1 = 0$. Concluding, if we neglect the Q_2 contribution, we get the final expression

$$\beta\mu_1(N_t, X) = -\ln \frac{Q_1 + Q_2}{Q(N_t, X)} \cong -\ln \frac{Q_1}{Q(N_t, X)}, \quad (\text{A. 13})$$

so that using Eq. (A. 10), Eqs. (40) and (41) are recovered.

-
- [1] J. Howard, *Mechanics of Motor Proteins and the Cytoskeleton* (Sinauer, Sunderland, MA, 2001)
 - [2] T. L. Hill, Proc. Natl. Acad. Sci. USA **78**, 5613 (1981)
 - [3] T. L. Hill and M. W. Kirschner, Proc. Natl. Acad. Sci. USA **79**, 490 (1982)
 - [4] M. J. Footer, J. W. J. Kerssemakers, J. A. Theriot, and M. Dogterom, Proc. Natl. Acad. Sci. USA **104**, 2181 (2007)
 - [5] C. Brangbour, O. du Roure, E. Helfer, D. Démoulin, A. Mazurier, M. Fermigier, M. Carlier, J. Bibette, and J. Baudry, PLoS Biol. **9**, e1000613 (2011)
 - [6] A. Reymann, J. Martiel, T. Cambier, L. Blanchoin, R. Boujemaa-Paterski, and M. Théry, Nature Mater. **9**, 827 (2010)
 - [7] A. Mogilner and G. Oster, Biophys. J. **71**, 3030 (1996)
 - [8] K. Tsekouras, D. Lacoste, K. Mallick, and J. Joanny, New J. Phys. **13**, 103032 (2011)
 - [9] A. Mogilner, J. Math. Biol. **58**, 105 (2009)
 - [10] J. Krawczyk and J. Kierfeld, EPL **93**, 28006 (2011)
 - [11] A. Gholami, M. Falcke, and E. Frey, New J. Phys. **10**, 033022 (2008)
 - [12] K. Guo, J. Shillcock, and R. Lipowsky, J. Chem. Phys. **131**, 015102 (2009)
 - [13] K. Guo, J. Shillcock, and R. Lipowsky, J. Chem. Phys. **133**, 155105 (2010)
 - [14] K. Lee and A. J. Liu, Biophys. J. **95**, 4529 (2008)
 - [15] K. Lee and A. J. Liu, Biophys. J. **97**, 1295 (2009)
 - [16] M. Caby, P. Hardas, S. Ramachandran, and J.-P. Ryckaert, J. Chem. Phys. **136**, 114901 (2012)
 - [17] J. Ryckaert and S. Ramachandran, Mol. Phys. (2013)
 - [18] A. Gholami, J. Wilhelm, and E. Frey, Phys. Rev. E **74**, 041803 (2006)
 - [19] T. L. Hill, *An Introduction to Statistical Thermodynamics* (Dover, New York, 1986)
 - [20] S. K. Kumar, I. Szleifer, and A. Panagiotopoulos, Phys. Rev. Lett. **66**, 2935 (1991)
 - [21] A. E. Carlsson, Biophys. J. **81**, 1907 (2001)
 - [22] A. Mogilner and B. Rubinstein, Biophys. J. **89**, 782 (2005)
 - [23] H. Yamakawa, *Modern Theory of Polymer Solutions* (Harper-Row, New York, 1971)
 - [24] D. A. McQuarrie, *Statistical Mechanics* (Harper-Row, New York, 1976)
 - [25] E. Gerritsma and P. Gaspard, Biophys. Rev. Lett. **5**, 163 (2010)